



**US Army Corps
of Engineers®**
Engineer Research and
Development Center

ERDC
INNOVATIVE SOLUTIONS
for a safer, better world

Engineering for Polar Operations, Logistics, and Research (EPOLAR)

Vertical Temperature Simulation of Pegasus Runway, McMurdo Station, Antarctica

Steven F. Daly, Robert Haehnel, and Christopher Hiemstra

January 2015



The U.S. Army Engineer Research and Development Center (ERDC) solves the nation's toughest engineering and environmental challenges. ERDC develops innovative solutions in civil and military engineering, geospatial sciences, water resources, and environmental sciences for the Army, the Department of Defense, civilian agencies, and our nation's public good. Find out more at www.erdc.usace.army.mil.

To search for other technical reports published by ERDC, visit the ERDC online library at <http://acwc.sdp.sirsi.net/client/default>.

Vertical Temperature Simulation of Pegasus Runway, McMurdo Station, Antarctica

Steven F. Daly, Robert Haehnel, and Christopher Hiemstra

*Cold Regions Research and Engineering Laboratory (CRREL)
U.S. Army Engineer Research and Development Center
72 Lyme Road
Hanover, NH 03755-1290*

Final Report

Approved for public release; distribution is unlimited.

Prepared for National Science Foundation, Division of Polar Programs,
Antarctic Infrastructure and Logistics
Arlington, VA 22230

Under Engineering for Polar Operations, Logistics, and Research (EPOLAR)
EP-ANT-14-51, "McMurdo Airfields Engineering Support, Continuation"

Abstract

Pegasus Runway, located 13 km south of McMurdo Station, Antarctica, on the McMurdo Ice Shelf (MIS), is constructed out of snow and ice. It is susceptible to weakening and damage caused by melting and to reduction in the strength caused by warm weather and sunlight. This report describes the development of the Pegasus Runway temperature model. It begins by quantitatively describing the physical properties of the Pegasus Runway snow and ice and the physical properties of the MIS directly beneath the runway. The temperature model is based on a one-dimensional heat conduction model that includes the penetration and absorption of solar radiation beneath the surface. The report describes the methods for estimating the sensible heat, latent heat, shortwave radiation, and long-wave radiation surface heat fluxes that drive the model and presents estimates of the constant-temperature lower-boundary condition for the model. A novel approach for estimating the initial vertical temperature profile is used. We simulate the Pegasus Runway temperatures for three austral summer seasons (2011–12, 2012–13, and 2013–14). The model simulation shows good results when compared to in situ observations of the runway temperatures.

DISCLAIMER: The contents of this report are not to be used for advertising, publication, or promotional purposes. Citation of trade names does not constitute an official endorsement or approval of the use of such commercial products. All product names and trademarks cited are the property of their respective owners. The findings of this report are not to be construed as an official Department of the Army position unless so designated by other authorized documents.

DESTROY THIS REPORT WHEN NO LONGER NEEDED. DO NOT RETURN IT TO THE ORIGINATOR.

Contents

Abstract	ii
Illustrations	v
Preface	vii
Acronyms and Abbreviations	viii
Unit Conversion Factors	ix
1 Introduction	1
2 Pegasus Runway	5
2.1 Overview	5
2.2 Snow and ice properties of Pegasus Runway.....	5
2.2.1 Snowcap	7
2.2.1.1 Density.....	7
2.2.1.2 Thermal conductivity.....	8
2.2.1.3 Heat capacity.....	9
2.2.1.4 Surface albedo	9
2.2.1.5 Solar radiation extinction.....	11
2.2.2 Superimposed ice	12
2.2.2.1 Density.....	12
2.2.2.2 Thermal conductivity.....	12
2.2.2.3 Heat capacity.....	13
2.2.2.4 Solar radiation extinction.....	13
2.2.3 Firn	13
2.2.3.1 Density.....	13
2.2.3.2 Thermal properties.....	15
2.2.4 Brine-saturated firn	16
2.2.5 Summary of snow and ice properties	18
3 Temperature Estimation	21
3.1 Heat conduction model	21
3.1.1 Solar radiative flux	22
3.1.2 Impact of meltwater on physical properties	23
3.2 Net surface heat flux	23
3.2.1 Overview	23
3.2.2 Sensible and latent heat fluxes.....	24
3.3 Lower thermal boundary condition	28
3.4 Initial temperature profile.....	30
4 Operational Field Data	32
5 Application	34
5.1 2011-12 season.....	36

5.2	2012–13 season.....	40
5.3	2013–14 season.....	44
6	Summary.....	48
References		51

Report Documentation Page

Illustrations

Figures

1	Pegasus Runway.....	2
2	Measured density of the snowcap	7
3	Measured and modeled snow surface albedo with solar angle.....	10
4	Bulk extinction coefficient for Antarctic snow.....	11
5	Observed firn density of MIS with depth (Kovacs et al. 1982).....	14
6	Observed firn density of MIS with overburden pressure (Kovacs et al. 1982)	15
7	Observed density with depth, and Pegasus Model density.....	19
8	Estimated thermal conductivity for each observed density, and Pegasus Model thermal conductivity.....	19
9	Estimated bulk extinction coefficient for each observed density, and Pegasus Model bulk extinction coefficient	20
10	Observed annual cycle of daily average temperatures at McMurdo Station with fitted period estimation	29
11	Estimated temperature profile throughout the MIS beneath the Pegasus Runway	30
12	View of the trench used for installing temperature sensors in the runway	33
13	Meteorological conditions during the 2011–12 season	37
14	Observed runway temperatures during the 2011–12 season	38
15	Modeled temperatures in the runway during the 2011–12 season.....	38
16	Observed and modeled temperature at a 4 in. depth	39
17	Modeled temperature and liquid water fraction at the surface	39
18	Meteorological conditions during the 2012–13 season	41
19	Observed temperatures in the runway during the 2012–13 season	42
20	Modeled temperatures in the runway during the 2012–13 season	42
21	Observed and modeled temperature at a 4 in. depth	43
22	Modeled temperature and liquid water fraction at the surface	43
23	Meteorological conditions during the 2013–14 season	44
24	Observed temperatures in runway during 2013–14 season.....	46
25	Modeled temperatures in runway during 2013–14 season	46
26	Observed and modeled temperature at a 4 in. depth	47
27	Modeled temperature and liquid water fraction at the surface	47

Tables

1	Measured brine-saturated firn properties.....	17
2	Values of the coefficients to use in equation (25)	27
3	Simulation periods	34

4	Model Parameters.....	35
5	Error statistics for the 2011–12 season.....	40
6	Error statistics for the 2012–13 season.....	41
7	Error statistics for the 2013–14 season.....	45

Preface

This study was conducted for the National Science Foundation (NSF), Division of Polar Programs (PLR), under Engineering for Polar Operations, Logistics, and Research (EPOLAR) EP-ANT-14-51, "McMurdo Airfields Engineering Support, Continuation." The technical monitor was George Blaisdell, Chief Program Manager, NSF-PLR, U.S. Antarctic Program.

The work was performed by Dr. Steven F. Daly (Remote Sensing/GIS and Water Resources Branch, Timothy Pangburn, Chief) and Dr. Robert Haehnel and Dr. Christopher Hiemstra (Terrestrial and Cryospheric Sciences Branch, Stephen Gaughan, Acting Chief), U.S. Army Engineer Research and Development Center, Cold Regions Research and Engineering Laboratory (ERDC-CRREL). At the time of publication, Dr. Lindamae Peck was Acting Chief of the Research and Engineering Division. The Deputy Director of ERDC-CRREL was Dr. Lance Hansen, and the Director was Dr. Robert Davis.

Dr. Robert Davis provided the cover photo.

COL Jeffrey R. Eckstein was Commander of ERDC, and Dr. Jeffery P. Holland was the Director.

Acronyms and Abbreviations

CRREL	U.S. Army Cold Regions Research and Engineering Laboratory
EPOLAR	Engineering for Polar Operations, Logistics and Research
ERDC	Engineer Research and Development Center
GPR	Ground-Penetrating Radar
MIS	McMurdo Ice Shelf
NSF	National Science Foundation
PIR	Precision Infrared Radiometer
PLR	Division of Polar Programs
PSP	Precision Spectral Pyranometer
SPAWAR	Space and Naval Warfare Systems Command

Unit Conversion Factors

Multiply	By	To Obtain
degrees (angle)	0.01745329	radians
feet	0.3048	meters
inches	0.0254	meters
microns	1.0 E-06	meters

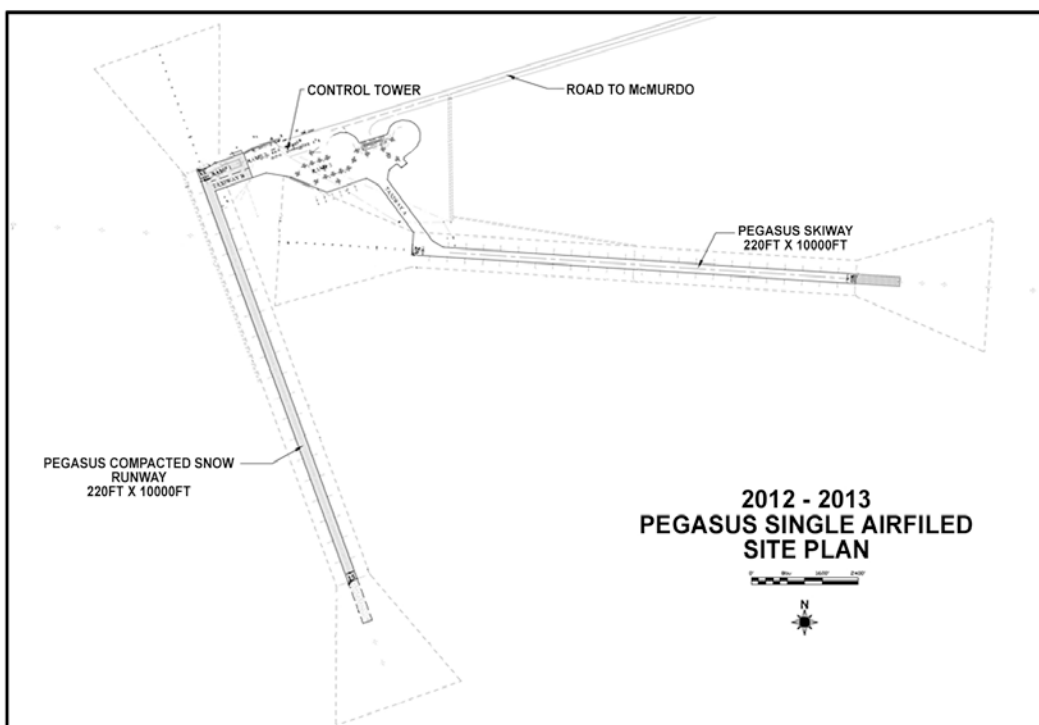
1 Introduction

The Pegasus Runway, intended for heavy wheeled aircraft, was constructed of snow and ice in the austral summer of 1992–93. It is located 13 km south of McMurdo Station, Antarctica, on the McMurdo Ice Shelf (MIS), a lobe on the extreme west of the Ross Ice Shelf. The area was selected after extensive study (for an overview, see Blaisdell et al. [1998] and also Mellor [1988] and Mellor and Swithinbank [1989]) and has unique snow cover and glaciological characteristics (Stuart and Bull 1963; Paige 1968; Swithinbank 1970) that are favorable for a permanent airfield (Klokov and Diemand 1995). The area where the runway was constructed has a “thin, but permanent and complete, snow cover” (Blaisdell and Lang 1995). The 3000 by 90 m runway was constructed in several steps to remove the rough surface ice, to fill low areas and subsurface melt holes, and to grade the runway flat and smooth (Blaisdell and Lang 1995). During subsequent seasons, the winter snowfall was used to cover the ice runway and to provide a high albedo protective layer, or “snowcap,” for the glacial ice. The snowcap is a layer of snow compacted and allowed to sinter so that it is strong enough to support wheeled aircraft.

The Pegasus Runway has been used each season since 1993. It has served as one of three airfields for the U.S. Antarctic Program air support system at McMurdo Station, which also includes the Sea Ice Runway, located on the sea ice in McMurdo Sound, and Williams Field, located on the snow-fields east of Pegasus on the Ross Ice Shelf. In most years, air operations at McMurdo Station have used the Sea Ice Runway early in the season with a switch over to Pegasus and Williams Field in late November to early December when the sea ice is no longer competent enough to support large cargo planes such as the C-17. Typically, Pegasus Runway has handled intercontinental flights of heavier wheeled aircraft originating from Christchurch, New Zealand, while ski equipped aircraft (e.g., LC-130s) have operated out of Williams Field. In 2009–10, a skiway was constructed at Pegasus (Figure 1); and the Sea Ice Runway and Pegasus were operated sequentially during the summer with both wheeled and ski-equipped aircraft using each airfield. During this time, Williams Field was minimally prepared to serve as an emergency divert landing site for ski-equipped aircraft. (See Haehnel et al. [2013] for a more thorough review of air operations at McMurdo Station). A critical part of efficient air operations is the

ability to use large capacity wheeled aircraft at McMurdo, such as the C-17, A-319, and B-757, to bring cargo and passengers from New Zealand and Australia while dedicating the slower and smaller ski-equipped LC-130s for transport of passengers and cargo from McMurdo to South Pole and to camps on the Antarctic continent. The Sea Ice Runway handles these wheeled flights early in the season when the temperatures are cold. During the warm part of the season (December and January), these wheeled flights are serviced at the glacial ice runway at Pegasus.

Figure 1. Pegasus Runway.



Given that the Pegasus Runway is constructed out of snow and ice, it is susceptible to weakening and damage caused by melting and to reduction in the strength of the snowcap caused by warm weather and solar radiation. The critical impact of solar radiation at the Pegasus Runway site has long been recognized. Paige (1968) describes subsurface melt pools that were discovered beneath blue glacier ice in the western part of MIS during a reconnaissance of this area for alternative airfields in the austral summer of 1965–66. He stated that the pools were caused by the greenhouse effect of intense solar radiation, low albedo of the blue glacier ice, and “heat absorption of dark objects.” Mellor and Swithinbank (1989) also described melt features in this area.

Because of these and other observations, there are a number of studies of the subsurface temperature regime in snow and ice in Antarctica (see, for example, Schlatter [1972], Brandt and Warren [1993], and Liston et al. [1999]). These studies' main focus has been to explain subsurface melting at below-freezing air and surface temperatures. In summary, these studies found that subsurface melting occurred in only blue glacier ice that was not snow covered. In snow-covered areas, the maximum of the vertical temperature profile could occur beneath the surface, and the maximum was limited to shallow depths with little or no subsurface melting. The differences between the conditions found in snow covered areas and those in areas of exposed blue ice could be explained "largely by radiative and heat-transfer interactions resulting from differences in albedo, grain-size, and density between the two mediums" (Liston et al. 1999). The ability of a surface snow cover to prevent subsurface melting was exploited at the Pegasus runway where it was found "by trial . . . that natural melt features could be prevented at the Pegasus site by completely covering exposed ice surfaces with . . . snow" (Blaisdell et al. 1998). In short, the protective properties of snow come from its ability to reflect most of the downwelling solar radiation and to effectively scatter the solar radiation that does penetrate the surface.

During the 2012–13 and 2013–14 seasons, Pegasus Runway experienced significant reductions in the strength of the snow and ice layers that composed the runway, leading to extended shutdowns. Also, during short warming trends that cause temporary reduction in the strength of the airfield, operations at the Pegasus Runway are shifted to the "night" when the sun is low in the sky and the ice is colder and stronger.

These disruptions to the runway operation have led to a program designed to forecast strength reductions of the snow and ice layers that compose the runway. The first step of this program was installing additional sensors at the Pegasus Runway. The meteorological station at Pegasus Runway was augmented with sensors to measure the downwelling broadband shortwave and long-wave radiation, two of the most important components of the surface heat balance. In addition, temperature sensors were placed at four locations in the Pegasus Runway to measure hourly temperatures at seven levels from 4 to 16 in. of depth. These measurements showed the runway temperatures were highly dynamic with large daily and seasonal variations.

The second step of this program was the development of a system to forecast the occurrence of strength reduction in the airfield. The two major components of the forecast system are a temperature model of the upper layers of the Pegasus Runway and a model of the runway strength. Separate reports will describe the runway strength model and the forecasting system. The present work describes the development of the temperature model of the upper layers of the Pegasus Runway. This report first describes the snow and ice properties of Pegasus Runway and the MIS directly below the runway. We next describe the development of the Pegasus Runway temperature model. This model is based on a one-dimensional heat conduction model and includes the penetration and absorption of solar radiation beneath the surface. We then describe the methods for estimating the heat fluxes that drive the model. These are sensible heat, latent heat, shortwave radiation, and long-wave radiation surface heat fluxes. Finally, we simulate the Pegasus Runway temperatures for three austral summer seasons (2011–12, 2012–13, and 2013–14).

2 Pegasus Runway

2.1 Overview

Pegasus Runway is constructed on the MIS, which moves in a generally northern and western direction (Swithinbank 1970) and periodically breaks off into McMurdo Sound. Haehnel et al. (2013) report the movement at the Pegasus Airfield to be about 30 m per year. Drilling in December 1991 found the ice shelf to be approximately 33 m thick at the north end of the Pegasus runway with 4.8 m of freeboard above sea level (Arcone et al. 1994). The bed of McMurdo Sound is roughly 600 m below sea level in this area.

The area of MIS east of Pegasus is an accumulation zone where more snow falls in a typical year than ablates. The annual accumulation gradually decreases moving westward towards Pegasus Runway, becoming zero at the transition from the accumulation area to the ablation area (Mellor and Swithinbank 1989; Swithinbank 1970). This transition zone, about 2 km wide and running in a north–south direction, was the location chosen for the Pegasus Runway. The snow cover in the transition zone “varies from local patches near the ablation region to over a meter where it phases into the accumulation zone. The Pegasus runway was sited just to the accumulation side of where the snow cover ceases to be patchy” (Blaisdell et al. 1998). The transition zone is also referred to as the *zone of superimposed ice* due to the extensive melting during some summers and subsequent re-freezing at the same location (Klokov and Diemand 1995); the Pegasus runway is located on superimposed ice (Blaisdell et al. 1998).

2.2 Snow and ice properties of Pegasus Runway

To model the temperatures in the Pegasus runway, it is necessary to have a description of density, thermal conductivity, specific heat, and the broadband shortwave radiation extinction of the snow and ice that compose and underlay the runway. The surface albedo must be known as well. It is not necessary that the numerical model extends through the entire vertical thickness of the MIS at the Pegasus Runway, only that the model extends to a depth at which a temperature boundary condition can be set. Typically, one would expect the temperature to be relatively constant and equal to the average annual air temperature at a depth of about 10–15 m below the

surface. However, the MIS thickness is finite with a lower boundary temperature determined by the ice–water interface temperature, a temperature much warmer than the average annual air temperature. That means that it is necessary to consider the conditions throughout the entire MIS thickness to estimate a temperature boundary condition beneath Pegasus.

Measurements of the physical properties in the field are limited to snow and ice density along with a few observations of broadband shortwave radiation extinction. We estimate the other properties based on the density and the ice type. The direct measurements of density made at the runway by us and by others were confined to the top 5 m. We infer the density deeper than 5 m based on measurements made by others in the vicinity of the Pegasus Runway. The vertical profile under the Pegasus runway is basically superimposed ice underlain by firn. Firn is the intermediate stage in the transition from snow to ice. At the upper surface of the superimposed ice is the thin, artificially maintained snowcap. The underlying firn has two distinct layers: an upper “normal” (dry) firn layer and, beneath that, a layer of brine-saturated firn that extends downwards to the bottom of the MIS. In all, there are four distinct layers of snow and ice at the runway between the surface and the bottom of the MIS: snowcap, superimposed ice, firn, and brine-saturated firn.

As stated previously, measurements in 1991 found the ice shelf to be approximately 33 m thick at the north end of the Pegasus runway with 4.8 m of freeboard above sea level. This thickness is consistent with the thickness map by McCrae (1984) and the recent airborne estimates of the MIS thickness by Rack et al. (2013). In general, the thickness of the MIS decreases with proximity to its northern ocean boundary. Kovacs et al. (1982) measured thicknesses of roughly 10–15 m within a kilometer of the edge and over 90 m about 10 km from the edge. The decrease in thickness towards the Ross Sea is apparently caused by ablation due to the intrusion of warm surface water beneath the MIS during the austral summer months (Stern et al. 2013). In contrast, Rack et al. (2013) detected ice platelet layers below the ice shelf in the areas of greatest thickness, indicating areas of basal freezing and supercooled water emerging from below the central ice shelf cavity into McMurdo Sound.

2.2.1 Snowcap

2.2.1.1 Density

The snowcap on the runway surface is approximately 27 cm thick. It is regularly compacted, planed, and dragged throughout the summer months of November through January to maintain a highly reflective, porous surface. We made measurements of the density of the snowcap as a function of depth at 18 locations along the length and width of the runway during 18–27 December 2011. These measurements extended to a depth of 40 cm and included both the snowcap (top 10–12 cm) and underlying ice. Figure 2 presents this data; a least-squares fit to the data is

$$\rho_s = (\rho_{ice} - \rho_0)(1 - e^{-\kappa z}) + \rho_0 \quad (1)$$

where

ρ_s = snowcap density (kg m^{-3});

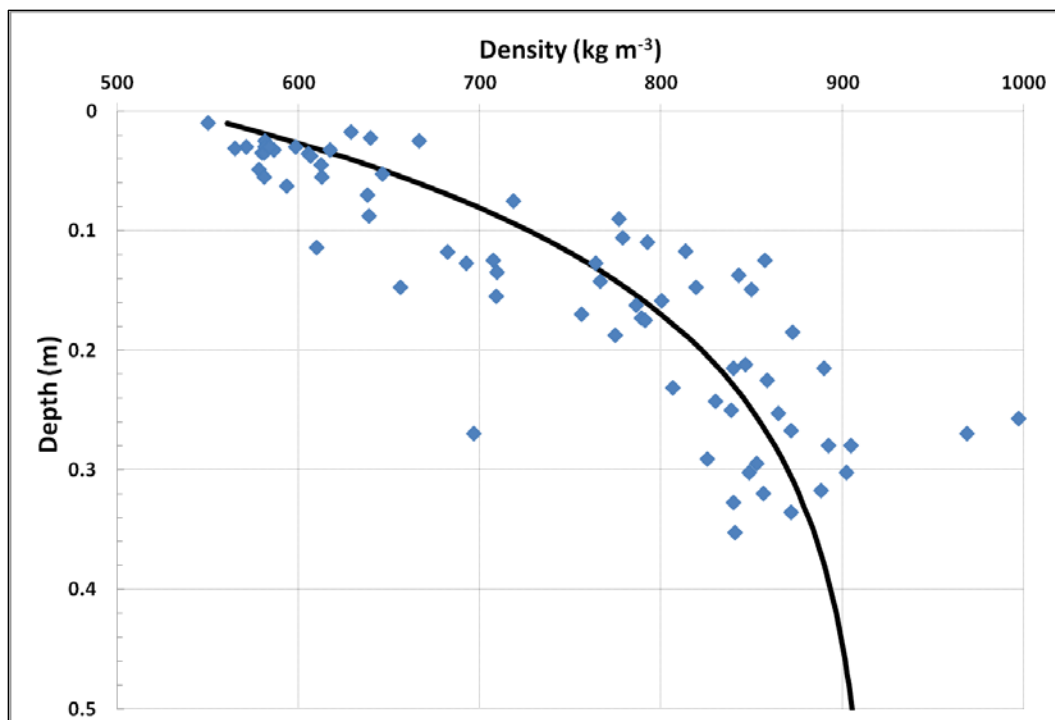
ρ_0 = 535.05 (kg m^{-3});

ρ_{ice} = density of ice, 917 (kg m^{-3});

z = depth (m);

κ = 6.98 (m^{-1}).

Figure 2. Measured density of the snowcap.



Two of the measurements indicate densities greater than the density of ice, 917 kg m^{-3} . It is likely that these samples contained sediments that have a density greater than ice. While overall sediment content of the snowcap is not known, sediment has a significant presence on the MIS; the far western edge of the MIS is heavily covered with sediment and debris. Rack et al. (2013) estimate sediments accumulated at the surface and present within the ice shelf can add up to a layer thickness of 2 m in that area. Towards the eastern edge of the MIS, Dunbar et al. (2009) found an annual accumulation rate of $0.80 \text{ g m}^{-2} \text{ year}^{-1}$ of aeolian sediment onto the ice shelf surface. They attribute this to strong storms that carry unconsolidated sediment from snow-free areas to the south, such as Black Island.

2.2.1.2 Thermal conductivity

The thermal conductivity of heavily compacted snow is not known with any certainty. The density of the snowcap ranges from 550 to 856 kg m^{-3} . These values are greater than the samples used by Sturm et al. (1997) to develop their thermal conductivity relationship for seasonal snow. (In fact, they limited the application of their equation to snow densities less than 600 kg m^{-3} .) To account for the possible differences between the heat transfer properties of the Pegasus Runway snow cover and seasonal snow and to ensure that thermal conductivity transitioned smoothly to that of ice as the density increased above 600 kg m^{-3} , we propose the following:

for $\rho_s \leq 600 \text{ kg m}^{-3}$,

$$k_s = 0.138 - 1.01 \times 10^{-3} \rho_s + 3.233 \times 10^{-6} \rho_s^2, \quad (2)$$

and for $\rho_s > 600 \text{ kg m}^{-3}$,

$$k_s = m(\rho_s - 600) + k_{600}, \quad (3)$$

where

$$m = \frac{k_{ice} - k_{600}}{\rho_{ice} - 600},$$

k_s = the thermal conductivity of the compacted snow ($\text{W} [\text{m} \text{ }^{\circ}\text{C}]^{-1}$),

k_{600} = the thermal conductivity of snow with density 600 kg m^{-3} calculated using equation (2).

This approach provided similar results to the average of the lower and upper limits of thermal conductivity of firn provided by Paterson (1994).

2.2.1.3 Heat capacity

We set the specific heat of the snowcap, per unit mass, to equal that of ice, $2114 \text{ J (kg }^{\circ}\text{C)}^{-1}$.

2.2.1.4 Surface albedo

The albedo of the snow cover at the Pegasus Runway site was measured (M. Knuth*, pers. comm.) in 15-minute intervals from 29 October 2010 until 5 February 2011. Two broadband pyranometers (Eppley Precision Spectral Pyranometer) were mounted on a mast immediately adjacent to the runway. One measured downwelling radiation and the other upwelling radiation from the snow surface. The ratio of the upwelling to the downwelling is the albedo. Values influenced by snow or frost on the upward looking pyranometers were discarded. The albedo values varied throughout each day and had longer trends of slight decline or increase of up to thirty days length. The daily variation correlated well with the solar angle (Woolf 1968), as expected. The reasons for the longer trends were not investigated but probably resulted from changing snow conditions. The average albedo values by solar angle were well described by the parameterization proposed by Dickinson et al. (1986) (as described in Gardner and Sharp [2010]):

$$\alpha_t = \alpha_{\theta_z < 60^\circ} + \max \left[0, 0.4 \left(\frac{1 - \alpha_{\theta_z > 60^\circ}}{b} \right) \left(\frac{b+1}{1+2bu_t} - 1 \right) \right] \quad (4)$$

where

$\alpha_{\theta_z < 60^\circ}$ = the average albedo when the solar angle is less than 60° (found to be 0.76 in the present case),

b = a fitting constant equal to 0.1 in the present case,

u_t = the cosine of the solar angle.

Figure 3 summarizes the measurements and equation (4). The pyranometers are rated up to a solar angle of only 80° , and we ignored

* U.S. Army Cold Regions Research and Engineering Laboratory, Hanover, NH.

values measured at solar angles greater than this (the sun is low on the horizon).

Following the examples of Henneman and Stefan (1999) and Douville et al. (1995), the surface albedo is also reduced at a time constant rate when the liquid water fraction of the surface layer is greater than zero. An albedo reduction factor, α_{rf} , is subtracted from α_t to arrive at the effective surface albedo, α_{te} .

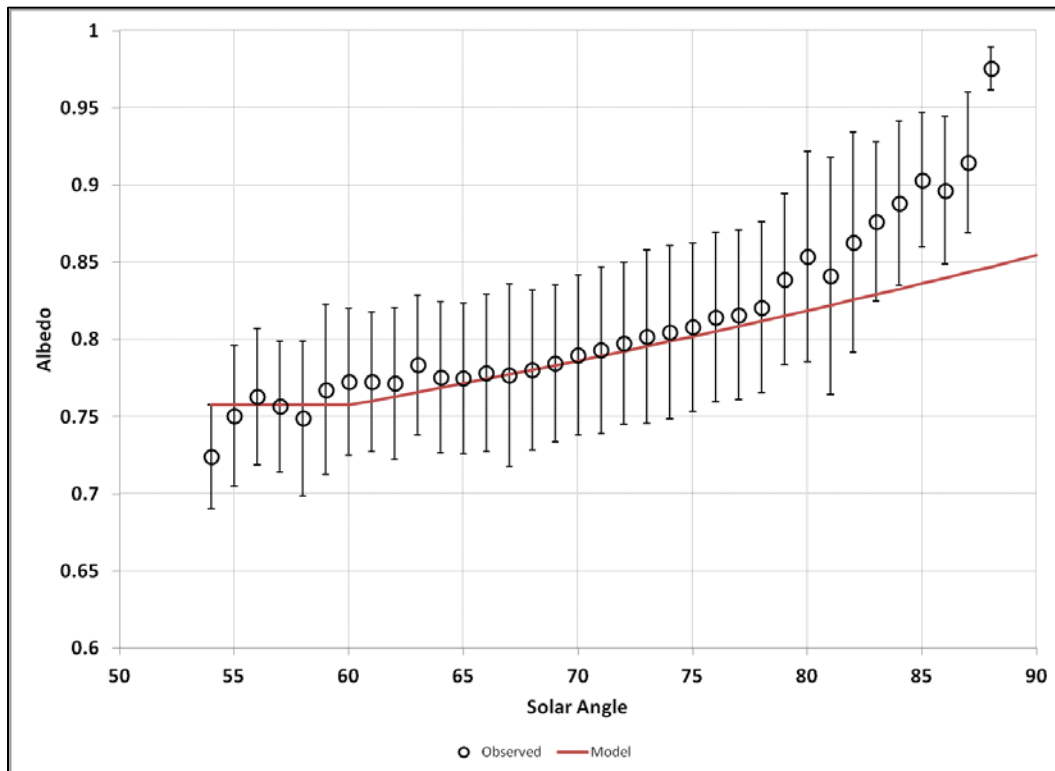
$$\alpha_{te} = \alpha_t - \alpha_{rf} \quad (5)$$

where

$$\alpha_{rf} = 0.068t_{melt} \quad (6)$$

and t_{melt} is the total time in days from the start of the time period with the melt fraction of the surface layer greater than zero. The factor 0.068 was determined empirically. If the melt fraction returns to zero, then α_{rf} is set to zero for the entire time that the melt fraction is zero. However, t_{melt} is not reset to zero.

Figure 3. Measured and modeled snow surface albedo with solar angle.



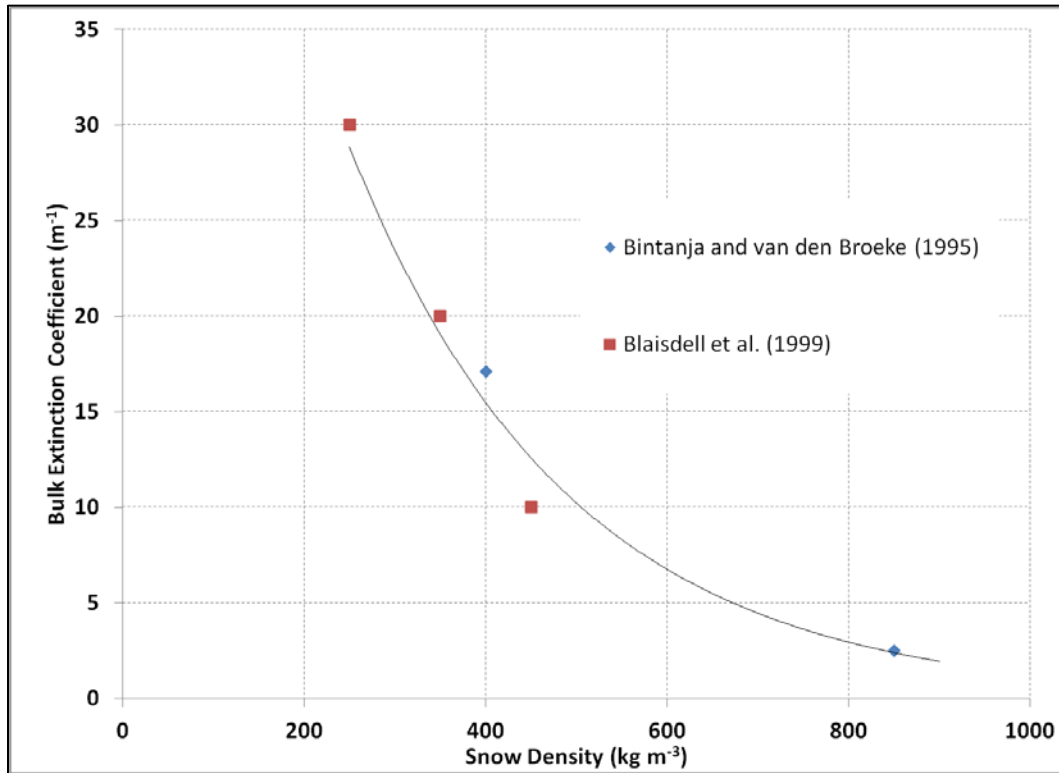
2.2.1.5 Solar radiation extinction

Blaisdell et al. (1998) measured bulk extinction coefficients for snow at the Pegasus site as 30 m^{-1} for snow with a density of approximately 250 kg m^{-3} , 20 m^{-1} for snow with a density of approximately 350 kg m^{-3} ; and 10 m^{-1} for snow with a density of approximately 450 kg m^{-3} . Bintanja and van den Broeke (1995) recorded two measurements for snow in Antarctica: 2.5 m^{-1} for snow with a density of 850 kg m^{-3} and 17.1 m^{-1} for snow with a density of 400 kg m^{-3} . Based on these measurements, we propose the following description of the bulk solar radiation extinction coefficient, μ (m^{-1}), as a function of the snow density:

$$\mu = 81.45e^{-0.004\rho_s}. \quad (7)$$

Figure 4 shows the results.

Figure 4. Bulk extinction coefficient for Antarctic snow.



2.2.2 Superimposed ice

2.2.2.1 Density

The superimposed ice, found immediately below the snowcap, is about 4.7 m thick. In January 1993, Arcone et al. (1994) conducted a ground-penetrating radar (GPR) survey of the superimposed ice, profiling the entire length of the runway along the western side. Solid and largely bubble-free ice was found in the top 2 m of ice in agreement with the ice core observations of Blaisdell et al. (1992). Arcone et al. (1994) detected a number of distinct linear horizons up to 30 m long, caused by density inhomogeneities resulting from of air bubbles trapped in the ice, between 3 and 7 m depth. As part of the survey, a 5 m ice core was removed from the runway and the ice density was measured at 0.10 m intervals. The ice density was at its maximum near the surface with a density very close to pure freshwater ice. The average density in the upper 4 m was 856 kg m^{-3} with a standard deviation of 25.8 kg m^{-3} (excluding anomalous layers). Two thin layers, approximately 0.10 m thick at 1.9 m and 3.7 m depth, were observed that had anomalously low densities of 600 kg m^{-3} or less. Arcone et al. (1994) assumed that these were representative of density inhomogeneities that caused the linear horizons seen in the radar profile. The density of the superimposed ice declined abruptly between 4.7 and 4.8 m depth to about 700 kg m^{-3} at 5 m depth. This represented the transition to the firn layer below.

2.2.2.2 Thermal conductivity

The density of the superimposed ice at Pegasus is less than pure ice due to the presence of air bubbles. The thermal conductivity of ice with air bubbles is estimated as (Schwerdtfeger [1963], as presented by Ashton [1986])

$$k_{ia} = \frac{(2k_{ice} + k_a)\rho_{ice} - 2(k_{ice} - k_a)(\rho_{ice} - \rho_{bi})}{(2k_{ice} + k_a)\rho_{ice} + (k_{ice} - k_a)(\rho_{ice} - \rho_{bi})} k_{ice} \quad (8)$$

where

k_{ia} = the conductivity of ice with air bubbles ($\text{W} [\text{m} \text{ }^{\circ}\text{C}]^{-1}$);

k_a = the thermal conductivity of air, $0.025 \text{ (W} [\text{m} \text{ }^{\circ}\text{C}]^{-1}\text{)}$;

ρ_{bi} = the density of ice including air bubbles.

This results in an estimate of $2.07 \text{ W (m }^{\circ}\text{C)}^{-1}$ for the thermal conductivity of the superimposed ice.

2.2.2.3 Heat capacity

We set the specific heat of the superimposed ice, per unit mass, to equal that of ice, $2114 \text{ J (kg }^{\circ}\text{C)}^{-1}$.

2.2.2.4 Solar radiation extinction

Grenfell and Maykut (1977) measured the bulk extinction coefficient of the penetrating fraction in freshwater ice to be 1.5 m^{-1} , which is similar to the value Liston et al. (1999) estimated, and is the value used here for the superimposed ice layer.

2.2.3 Firn

2.2.3.1 Density

The “normal” (dry) firn layer beneath the Pegasus Runway lies between 4.8 and 9 m depth. The MIS is composed predominately of firn. Kovacs et al. (1982) measured the vertical distribution of firn density at several locations on the MIS approximately 14 km to the northeast of Pegasus. Figure 5 shows the results of their measurements as a function of depth. Their measurements show the firn density increasing with depth, and all the measurements at all locations collapse to a single curve when plotted with depth. The sharp interface where they encountered the brine-saturated firn at each borehole is very apparent in the figure where the density abruptly increases at approximately the 10, 20, 35, and 50 m depths. Their density measurements in the dry firn are well described as a function of depth by

$$\rho_{firn} = (\rho_{ice} - \rho_0)(1 - e^{-\kappa z}) + \rho_0 \quad (9)$$

where

ρ_{firn} = firn density (kg m^{-3});

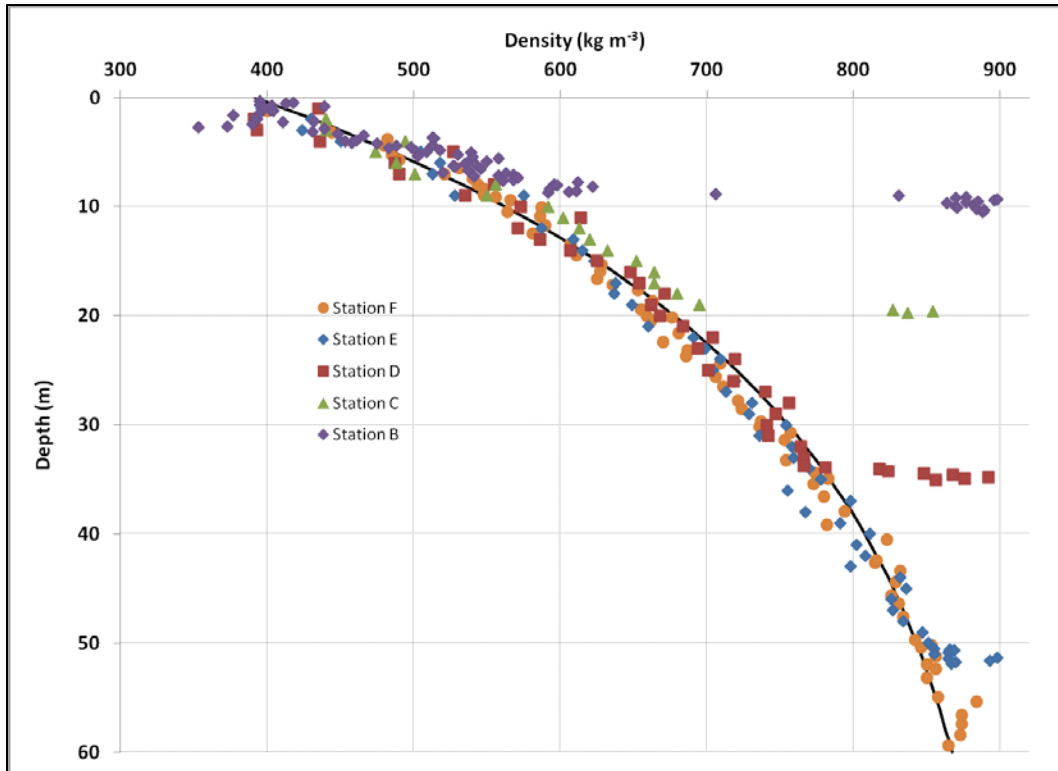
ρ_0 = $391.7 \text{ (kg m}^{-3}\text{)}$;

ρ_{ice} = density of ice, $917 \text{ (kg m}^{-3}\text{)}$;

z = depth (m);

κ = $0.0393 \text{ (m}^{-1}\text{)}$.

Figure 5. Observed firn density of MIS with depth (Kovacs et al. 1982).



However, we would not expect the density beneath the Pegasus Runway to exactly follow the density-depth curve shown in Figure 5. The overburden pressure caused by the superimposed ice on the underlying firn would be greater than the pressure exerted by firn of the same thickness and vertical position given the greater density of the superimposed ice compared to firn. Therefore we expect the overburden pressure to be a better indicator of firn density beneath the runway than depth beneath the surface would be. To describe the firn density as a function of the overburden pressure, we used the measurements of firn density by Kovacs et al. (1982) and estimates of the corresponding overburden pressure:

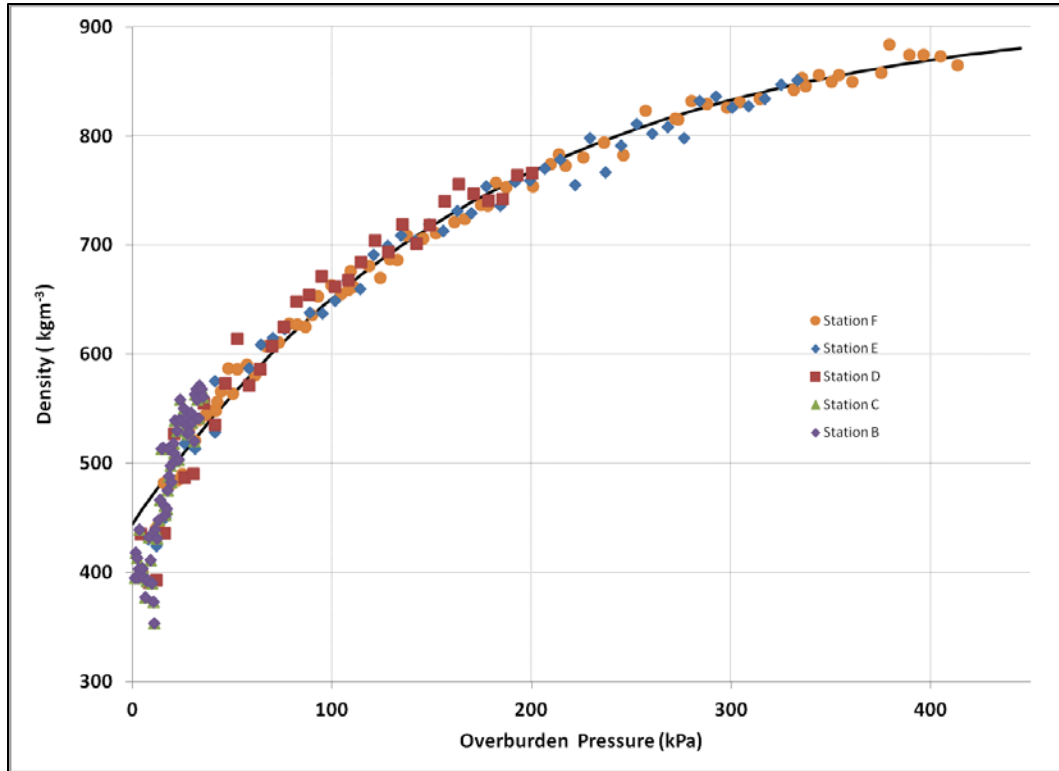
$$\rho_{firn} = (\rho_{ice} - \rho_0)(1 - e^{-KP}) + \rho_0 \quad (10)$$

where

$$\begin{aligned} \rho_0 &= 444.52 \text{ (kg m}^{-3}\text{),} \\ P &= \text{overburden pressure (kPa),} \\ K &= 0.00575 \text{ (kPa}^{-1}\text{)} \end{aligned}$$

Figure 6 shows these results; note that the data points influenced by brine have not been included with this graph.

Figure 6. Observed firn density of MIS with overburden pressure (Kovacs et al. 1982).



The overburden pressure at the bottom of the superimposed ice is roughly 39.2 kPa at 4.8 m depth. At this pressure, one would expect the firn density to be 540 kg m^{-3} based on equation (10). According to equation (9), this density would be found at a depth 8.5 m in the MIS. We estimated the density profile of the firn beneath the superimposed ice by adding 3.7 m (the difference between 4.8 m and 8.5 m) to the depth in equation (9) for every depth below the superimposed ice. Based on the GPR measurements of Arcone et al. (1994), we expect the transition to brine-saturated firn to occur at a 9 m depth.

2.2.3.2 Thermal properties

We assumed that the functions that described the thermal properties of the snowcap also apply for the thermal conductivity, specific heat, and bulk extinction coefficient of the normal firn layer.

2.2.4 Brine-saturated firn

The layer of brine-saturated firn extends from a depth of 9 m to the bottom of the MIS at a depth of 33 m. Brine-saturated firn was first detected in the MIS in 1959 (Heine 1968). The brine is understood to originate from seawater entering the seaward ice front of the MIS after breakout of the shelf ice into McMurdo Sound (Heine 1968; Risk and Hochstein 1967; Kovacs and Gow 1975; Kovacs et al. 1982; Cragin et al. 1983). Apparently, permeable ice does not exist at the bottom of the ice shelf; so brine cannot enter through the bottom of the MIS. As a result, the upper surface of the brine layer is consistently at a lower elevation than sea level; and the brine layer surface slopes downwards away from the ice front. Using GPR, Kovacs et al. (1982) detected step-like waves of propagating brine. Each wave corresponded to a specific breakout event. As the brine moves through the firn, it becomes more concentrated as water is removed by freezing, finally reaching concentrations of five and seven times that of the original seawater (Cragin et al. 1983).

Kovacs et al. (1982) mapped the limits of the brine penetration in the MIS. This map indicates that the location of Pegasus Runway is likely to be in the region of brine-saturated firn. Arccone et al. (1994) also confirmed this in their January 1993 GPR survey of the Pegasus runway site. The dominant feature of the survey was a strong reflection originating between 8 and 9 m of depth. Arccone et al. (1994) attributed this layer to brine that was contiguous with the brine layer identified to the east by Kovacs et al. (1982). We look to the measurements of Kovacs et al. (1982) for information on the densities of the brine-saturated firn (Table 1). First of all, the measurements show an abrupt increase of density at the interface between the dry firn and the brine-saturated firn. The data of Heine (as reported by McCrae 1984) also shows this abrupt transition. Kovacs et al. (1982) reported measured densities for three cores that penetrated the brine-saturated firn layer. The average values of the total density (brine and ice) ranged from 836.6 to 877.8 kg m⁻³ as shown in Table 1. Each of the cores indicates increasing density with depth within the brine-saturated firn layer. All the cores reach a maximum of about 880 kg m⁻³ 1 m below the top of the brine layer.

Table 1. Measured brine-saturated firn properties.

Location	Distance from MIS edge(m)	Brine Depth below Surface (m)	Brine Depth below Sea Level (m)	MIS Thickness (m)	Observed			Calculated (Cox and Weeks 1983)			
					Average Melt Salinity (PPT)	Average Temperature (C)	Total Density (kg m ⁻³)	Ice Fraction	Brine Fraction	Brine Salinity (PPT)	Air Fraction
Station B	800*	8.85	1	20	4.5	-3.50	877.8	0.891	0.058	61.3	0.051
High Side of Brine Step	2840	16.9	4.4	34	14	-14.72	889.1	0.896	0.058	174.5	0.049
Low Side of Brine Step	2900	21.5	8.8	35	25	-12.75	869.5	0.811	0.112	162.0	0.081
Station C	3590	19.4	9.8	40							
Station D	7370	33.8	13.2	68	8.3	-15.0	836.6	0.891	0.032	177	0.079
Station E	9560	50.4	24.1	84.6	4.2	-16.3	871.5	0.930	0.015	186	0.056
Station F	9700			88.5							

* estimated

We assume an abrupt transition to brine-saturated firn at a depth of 9 m beneath Pegasus runway as indicated by the GPR survey. At this depth, the density jumps abruptly from the firn density to that of the brine-saturated firn. At the upper surface of the brine, we assume a total density of 860 kg m⁻³ with a linear increase over the next meter of depth to a density of 880 kg m⁻³. There are a number of factors to take into account to estimate the thermal conductivity and specific heat of the brine-saturated firn. First, the presence of brine, ice, and air all impact the thermal conductivity and heat capacity (Schwerdtfeger 1963; Ono 1967; Yen et al. 1992). Unfortunately, we have no measurements of the actual properties of the brine-saturated firn beneath Pegasus Runway. We expect that the density of the original dry firn prior to flooding by the brine would follow the pattern described by equations (9) and (10). The salinity of the original brine that flooded this location is not known. As described by Cragin et al. (1983), the brine can become more concentrated as it moves through the firn; and the measurements of Kovacs et al. (1982) do not present a consistent picture of the original brine salinity. Freezing of the brine would form additional ice, and we expect that the fraction of ice would be greater than the original dry firn so that the thermal properties would largely reflect those of ice. However, it is well known that the presence of

brine can have a dramatic impact, especially on the heat capacity at warm temperatures and high salinities. We approximate the thermal properties based on the properties of ice with bubbles as described by equation (8). This approximation is justified given the 9 m depth of the top of the brine layer. This means that in regions where the temperature is changing and heat capacity is important, the ice is cold, and the brine has less impact on the thermal properties. Our calculations, discussed in Section 3.3 and 3.4, suggest that the temperature of the brine-saturated firn will be constant throughout the year below a depth of 15 m beneath the surface of the Pegasus Runway. We set the lower boundary of our simulation domain at 15 m where we can assume a constant temperature. We assumed that the thermal conductivity for the saturated brine layer above this depth was equivalent to that of ice with a density of 880 kg m^{-3} and calculated the thermal conductivity as $2.13 \text{ W (m }^{\circ}\text{C)}$ based on equation (8).

2.2.5 Summary of snow and ice properties

Figures 7 through 9 show the vertical profiles of density, thermal conductivity, and bulk extinction coefficients used in the Pegasus Model. The vertical density profile is the black line shown in Figure 7. The open symbols are the data points used to develop the line in each of the four sections. The dark green circles are the measurements of Kovacs et al. (1982) of the firn density near the Pegasus Runway. The open green circles are the data points modified to account for the additional overburden pressure of the superimposed ice.

The vertical thermal conductivity profile is the black line shown in Figure 8. The open symbols are the thermal conductivities calculated for the densities shown in Figure 7.

The vertical bulk extinction coefficient profile is the black line shown in Figure 9. The open symbols are the bulk extinction coefficients calculated for the densities shown in Figure 7. We expect minimal solar radiation to penetrate below 3 m of depth but show the bulk extinction coefficient profile down to 15 m as required by the model.

Figure 7. Observed density with depth, and Pegasus Model density.

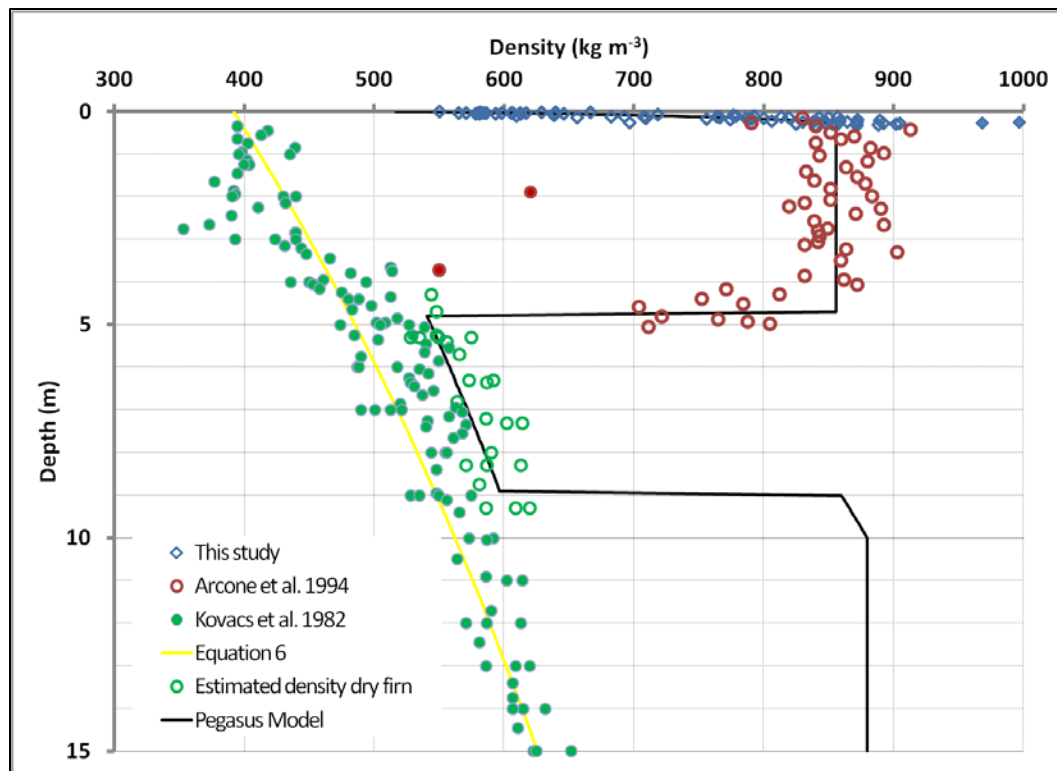


Figure 8. Estimated thermal conductivity for each observed density, and Pegasus Model thermal conductivity.

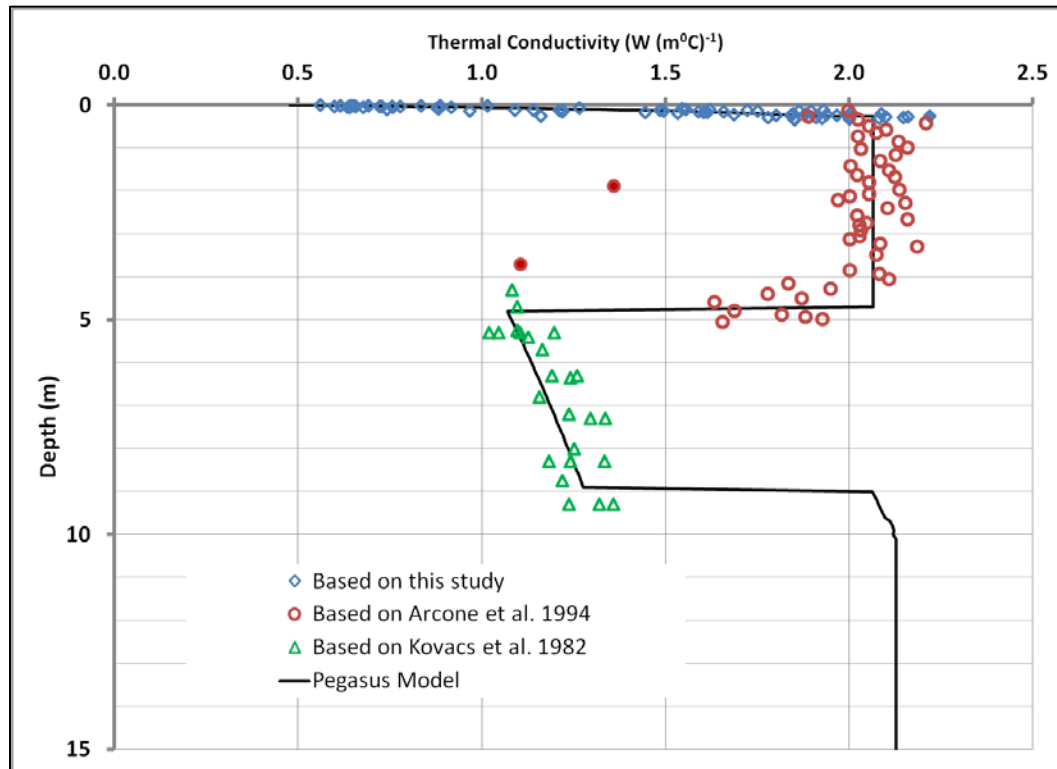
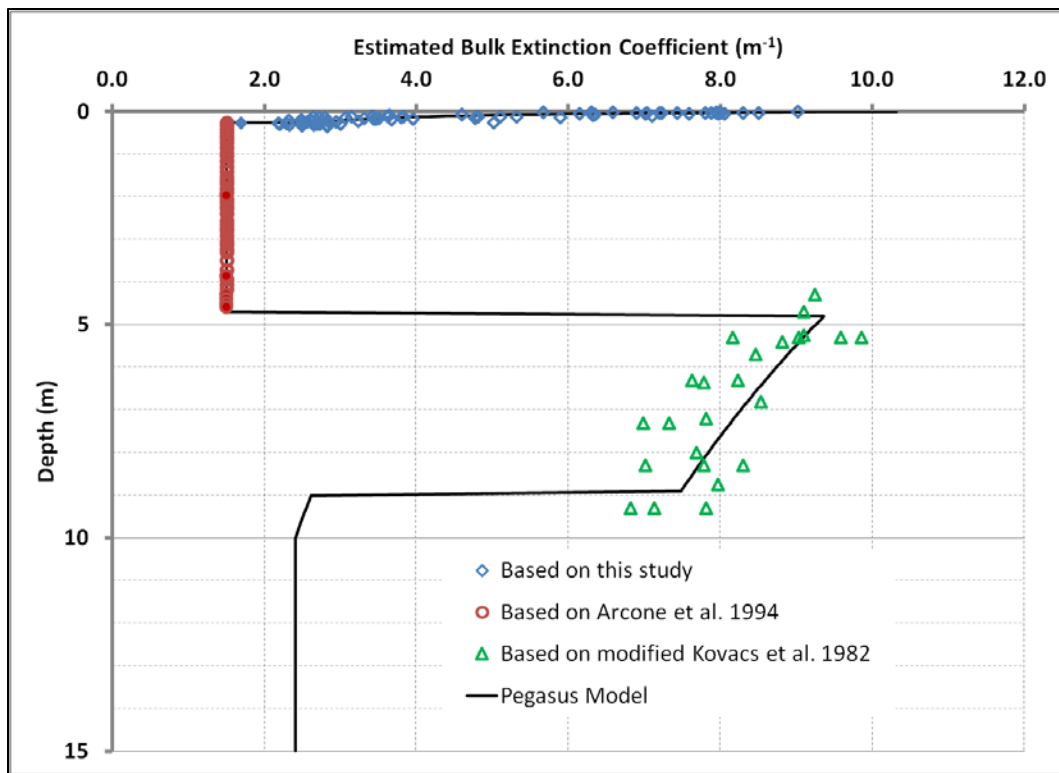


Figure 9. Estimated bulk extinction coefficient for each observed density, and Pegasus Model bulk extinction coefficient.



3 Temperature Estimation

There are several components required for estimating the vertical temperature distribution in the Pegasus Runway. The first component is the heat transfer model of the runway snowcap, superimposed ice, firn, and brine-saturated firn. The heat transfer model is based on a one-dimensional heat-conduction equation that includes internal heat generation through solar radiation absorption. Particular attention must be placed on the heat conduction parameters of density, thermal conductivity, and radiation absorption, which vary significantly with depth. The second component is estimating the model upper and lower boundary conditions. The energy flux absorbed at the surface forms the upper boundary condition of the heat conduction model. The lower boundary condition is a fixed temperature. A third component is the initial temperature profile that must be set at the start of each simulation period. We discuss each of these components below.

3.1 Heat conduction model

The temporal evolution of the vertical temperature distribution is described by the one-dimensional heat transfer equation:

$$\rho_i C_p \frac{\partial T_i}{\partial t} = \frac{\partial}{\partial z} \left[k_i \frac{\partial T_i}{\partial z} \right] + \frac{\partial Q_{swz}}{\partial z} \quad (11)$$

where

- T_i = the temperature of the i th snow or ice layer ($^{\circ}\text{C}$),
- z = the depth (m),
- t = time (s),
- ρ_i = the density of the i th snow or ice layer (kg m^{-3}),
- C_p = the specific heat ($\text{J} [\text{kg} ^{\circ}\text{C}]^{-1}$),
- k_i = the thermal conductivity ($\text{W} [\text{m} ^{\circ}\text{C}]^{-1}$),
- Q_{sw} = the solar radiative flux (W m^{-2}).

This heat conduction equation is solved using a Crank-Nicholson finite-difference scheme following the approach of Flato and Brown (1996). This approach allows for a variable solution grid that divides the snow and ice composing the runway and the MIS beneath the runway into layers of ar-

bitrary thickness. Each layer is assumed to have a uniform thermal conductivity and heat capacity. The model domain extends from the surface of the Pegasus Runway down to a depth of 15 m. The physical properties of the runway snow and ice are assumed known and summarized in Figures 7–9. The solution requires boundary conditions at the upper surface and at the bottom surface of the model domain and a known initial temperature distribution at the start of the simulation time period. The upper boundary condition is the net surface heat flux absorbed at the surface. The lower boundary condition is a constant, known temperature.

3.1.1 Solar radiative flux

It is well known that the albedo and absorption of solar radiation by snow and ice varies with wavelength. However, given the operational constraints at the Pegasus runway, only broadband solar radiative downwelling flux data is currently available or likely to be available in the future. The shortwave radiation absorption can be divided into two processes: the absorption at the surface of the non-penetrating fraction and the gradual absorption with depth of the penetrating fraction (Grenfell and Maykut 1977; Maykut 1982). At Pegasus Runway, the surface layer is snow; and the fraction of the shortwave radiation penetrating into snow is generally small. The penetrating fraction of the shortwave radiation, Q_{sw0} , can be estimated as

$$Q_{sw0} = \beta(1 - \alpha_{te})Q_{sw\downarrow} \quad (12)$$

where

- β = the penetrating fraction,
- $Q_{sw\downarrow}$ = the downwelling shortwave radiation (W m^{-2}),
- α_{te} = the effective broadband surface albedo.

The albedo, α_{te} , is a function of the solar angle as shown in equations (4) and (5) and is reduced by the presence of liquid water on the surface layer. The penetrating fraction is set at 0.17 following the example of Flato and Brown (1996) for thin snow.

The absorption of the penetrating fraction is described by the bulk extinction coefficient, which varies with depth as shown in Figure 9. The broad-

band absorption of the penetrating fraction of solar radiation absorption with depth is described by

$$Q_{swz} = Q_{sw0} e^{-\mu z} \quad (13)$$

where Q_{swz} is the flux of shortwave solar radiation at depth z in the snow-pack (W m^{-2}) and μ is the bulk extinction coefficient(m^{-1}).

3.1.2 Impact of meltwater on physical properties

The three physical properties of the snow and ice, ρ_i , C_p , and k_i , are all modified, following the example of Liston et al. (1999), when meltwater is present. The thermal conductivity is modified according to

$$k_{imelt} = (1 - f_w)k_i + f_w k_w \quad (14)$$

where

f_w = the water fraction ($1 \geq f_w \geq 0$),

k_i = the thermal conductivity of layer with no melt ($\text{W} [\text{m} \text{ }^{\circ}\text{C}]^{-1}$),

k_w = the thermal conductivity of water ($\text{W} [\text{m} \text{ }^{\circ}\text{C}]^{-1}$).

A similar procedure is followed for ρ_i and C_p .

3.2 Net surface heat flux

3.2.1 Overview

The net heat flux absorbed at the surface, F_o , serves as the upper boundary condition for the heat conduction model

$$k_i \left. \frac{\partial T}{\partial z} \right|_{surface} = F_o. \quad (15)$$

F_o is composed of four modes of heat transfer: the net long-wave and shortwave radiation; the latent heat flux, H_L ; and the sensible heat, H_S .

$$F_o = Q_{lw\downarrow} - \varepsilon\sigma T_s^4 + (1 - \alpha_{te})(1 - \beta)Q_{sw\downarrow} + H_L + H_S \quad (16)$$

where

- $Q_{lw\downarrow}$ = the downwelling long-wave radiation (W m^{-2}),
- T_s = the surface temperature ($^{\circ}\text{C}$),
- ε = the snow surface emissivity,
- σ = the Stefan–Boltzmann constant ($\text{W m}^{-2} \text{K}^{-4}$),
- α_t = the broadband shortwave surface albedo,
- B = the penetrating fraction of the shortwave radiation,
- $Q_{sw\downarrow}$ = the downwelling shortwave radiation (W m^{-2}).

Both $Q_{lw\downarrow}$ and $Q_{sw\downarrow}$ were measured at the Pegasus Runway.

3.2.2 Sensible and latent heat fluxes

Modern methods for estimating surface fluxes of sensible heat, H_s , and latent heat, H_L , from extensive, horizontally homogeneous snow and ice surfaces rely on a bulk flux algorithm (see Andreas [1996] for a complete review). The bulk flux algorithm must include predictions for all three turbulent fluxes—momentum, τ , and sensible and latent heat—because the prognostic equations are coupled. The basic equations are

$$\tau = \rho C_{Dr} S_r^2, \quad (17)$$

$$H_s = \rho_a C_{pa} C_{Hr} S_r (\Theta_s - \Theta_r), \quad (18)$$

$$H_L = \rho_a L_v C_{Er} S_r (Q_s - Q_r) \quad (19)$$

where

- S_r = wind speed at reference height r (m s^{-1});
- Θ_r and Q_r = the potential temperature ($^{\circ}\text{C}$) and specific humidity (kg kg^{-1}) of the air at r ;
- Θ_s and Q_s = the temperature ($^{\circ}\text{C}$) and specific humidity (kg kg^{-1}) of the air at the surface;
- ρ_a , C_{pa} , and L_v = the air density (kg m^{-3}), specific heat of air ($\text{J} [\text{kg} ^{\circ}\text{C}]^{-1}$), and latent heat of vaporization or sublimation (J kg^{-1}).

The temperature of the air at the surface is assumed to be equal to the surface temperature calculated by the heat conduction model. The specific humidity of the air at the surface is determined by the saturation vapor

pressure over ice at the calculated surface temperature and observed air pressure (Andreas 2005).

The key to using equations (17), (18), and (19) is estimating the drag coefficient appropriate at reference height r (C_{Dr}) and the transfer coefficients for sensible (C_{Hr}) and latent (C_{Er}) heat at r . These are obtained by estimating the roughness lengths for wind speed (z_0), temperature (z_T), and humidity (z_Q) (e.g., Andreas 1998):

$$C_{Dr} = \frac{k^2}{[\ln(r/z_0) - \psi_m(r/L)]^2}, \quad (20)$$

$$C_{Hr} = \frac{k^2}{[\ln(r/z_0) - \psi_m(r/L)][\ln(r/z_T) - \psi_h(r/L)]}, \quad (21)$$

$$C_{Er} = \frac{k^2}{[\ln(r/z_0) - \psi_m(r/L)][\ln(r/z_Q) - \psi_h(r/L)]}. \quad (22)$$

Here,

$k = 0.4$, the von Kármán constant;
 L = the Obukhov length, a stratification parameter (m);
 ψ_m and ψ_h = known functions of r/L .

For ψ_m and ψ_h , we use Paulson's (1970) functions for unstable stratification (i.e., for $L < 0$) and Holtslag and De Bruin's (1988) (see also Andreas [1998]) for stable stratification (i.e., for $L > 0$).

The Obukhov length is a stratification parameter; in the algorithm, we compute it as

$$L = -\frac{\overline{\Theta}}{k g} \left(\frac{u_*^2}{t_* + \frac{0.61\overline{\Theta}}{1 + 0.61\overline{Q}} q_*} \right). \quad (23)$$

Here,

- u_* = friction velocity (m s^{-1});
- t_* = surface layer temperature scale, $\frac{H_s}{\rho_a C_{pa} u_*}$ ($^{\circ}\text{C}$);
- q_* = surface layer humidity scale, $\frac{H_L}{\rho_a L_v u_*}$ (kg kg^{-1});
- g = gravity (m s^{-2});
- $\bar{\Theta}$ = the surface layer mean temperature ($^{\circ}\text{C}$);
- \bar{Q} = the surface layer mean humidity (kg kg^{-1}).

For the snow- and ice-covered area of the Pegasus site, we use a constant value for z_0 , 1 mm. This is a typical value for snow-covered ice (e.g., Andreas and Claffey 1995). For z_T and z_Q in equations (21) and (22), we use Andreas's (1987) parameterization. This, likewise, has proven useful for estimating heat and vapor fluxes over surfaces of ice or snow (e.g., Jordan et al. 1999, 2001).

The Liu et al. (1979) and Andreas (1987) models are somewhat similar in their approaches to predicting the roughness lengths for temperature and moisture, z_T and z_Q . Both of these define a roughness Reynolds number as

$$R_* = \frac{u_* z_0}{\nu}. \quad (24)$$

This is formed like the usual Reynolds number—a velocity scale times a length scale divided by the kinematic viscosity of the air, ν . Here, however, the velocity and length scales are related to the friction velocity and z_0 .

The Andreas (1987) model predicts the scalar roughness length, z_s (either z_T or z_Q), from

$$\ln(z_s/z_0) = b_0 + b_1 \ln R_* + b_2 (\ln R_*)^2, \quad (25)$$

where Table 2 gives the polynomial coefficients (also tabulated in Andreas [1987, 2002]).

Table 2. Values of the coefficients to use in equation (25).

Coefficient	$R_* \leq 0.135$	$0.135 < R_* < 2.5$	$2.5 \leq R_* \leq 1000$
	Smooth	Transition	Rough
Temperature (z_T/z_0)			
b_0	1.250	0.149	0.317
b_1	0	-0.550	-0.565
b_2	0	0	-0.183
Humidity (z_0/z_0)			
b_0	1.610	0.351	0.396
b_1	0	-0.625	-0.512
b_2	0	0	-0.180

Finally, we need to discuss the wind speed variable, S_r , in equations (17), (18), and (19). When the stratification is unstable, we model S_r by using the COARE gustiness parameterization (Fairall et al. 1996):

$$S_r^2 = U_r^2 + \beta^2 w_*^2. \quad (26)$$

Here,

U_r = the wind speed measured at reference height r (m s^{-1}),
 w_* = the convective velocity scale (m s^{-1}) (e.g., Deardorff 1970;

Fairall et al. 1996),

$\beta = 1.25$.

Equation (26) acknowledges that, in unstable stratification, convectively driven atmospheric motions still cause turbulent transport even when the mean winds are light.

Similarly, in stable stratification, we model S_r as

$$S_r = U_r + W_0, \quad (27)$$

where W_0 is a so-called windless parameter that we take as 0.5 m s^{-1} (Jordan et al. 1999). Like equation (26), equation (27) acknowledges that, even when the mean wind speed approaches zero, in stable stratification the atmosphere still has ways to carry out vertical exchange. In a stably stratified atmosphere, gravity waves are probably the main agents for this “windless” exchange.

Many of the equations in our algorithm are coupled because they depend on u_* . The Obukhov length L that appears in (23) is the main coupling variable, though, because it contains u_* , H_s , and H_L . Thus, we must solve this system of equations iteratively by first assuming neutral stratification (i.e., $r/L = 0$) and then iteratively calculating the actual value of L .

3.3 Lower thermal boundary condition

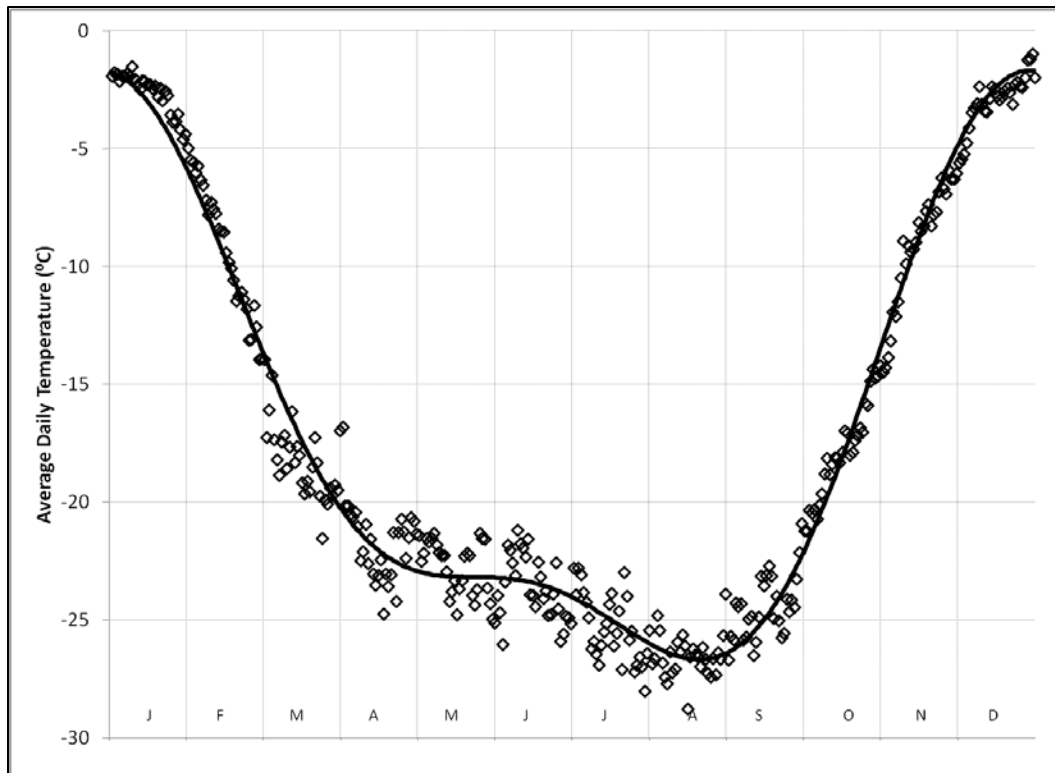
The lower thermal boundary condition is set as a constant temperature at the maximum depth of the solution domain. This is the minimum depth at which the ice temperature is constant throughout the simulation period. There are no measurements of the temperature deep beneath the runway to use as a guide for selecting the depth. To estimate the minimum depth with constant temperature, we solved equation (11) for the temperature profile through the entire thickness of the MIS beneath the Pegasus Runway. This simulation used a simplified surface heat flux calculation that assumed that the surface temperature was equal to the air temperature and that the air temperature throughout each year could be estimated using cosine functions. First, to determine the cosine functions, the average daily temperature of each day of the year at the McMurdo station was calculated based on the period of record (1973 to the present). Then, the annual cycle of temperatures was estimated using cosine functions. We found that only two periods were necessary to provide a very reasonable fit to the data as shown in Figure 10. The average temperature on day j , T_j , is found as

$$T_j = \bar{T} + \sum_{n=1}^2 A_n \cos\left(\frac{n2\pi j}{365} - \varepsilon_n\right) \quad (28)$$

where

- j = the Julian day of the year,
- \bar{T} = the annual average temperature at McMurdo Station (-17.04°C),
- A_n = the amplitude of the n th cycle ($A_1 = 11.19^{\circ}\text{C}$, $A_2 = 4.29^{\circ}\text{C}$),
- ε_n = the phase of the n th cycle ($\varepsilon_1 = 0.08$, $\varepsilon_2 = -0.27$).

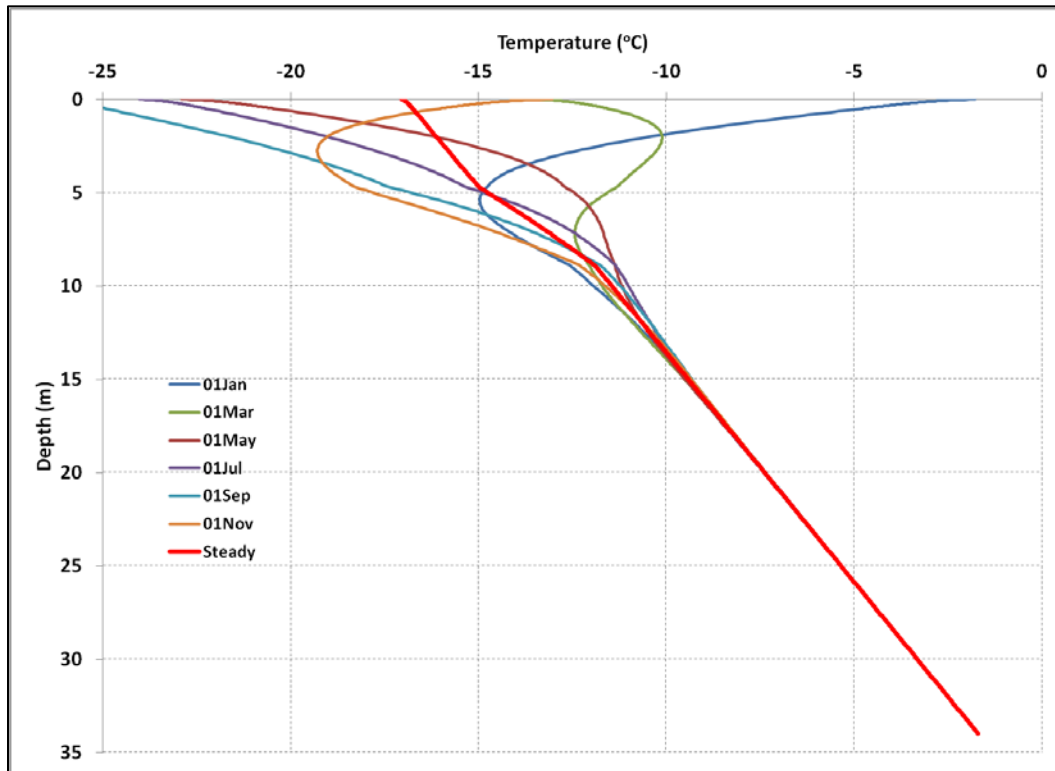
Figure 10. Observed annual cycle of daily average temperatures at McMurdo Station with fitted period estimation.



The vertical temperature profile was estimated using one-day time steps. The physical characteristics used were as described above, and the conditions at 15 m were extended to the bottom of the MIS at 34 m depth. The thermal boundary condition at the bottom of the MIS was fixed at the ice/sea water equilibrium temperature of -1.7°C . The simulation started with the initial vertical profile temperature set at the annual average air temperature of -17.04°C . After simulating 30 years, during which the surface temperature was varied according to equation (28), the results showed that the temperature in the upper portion of the MIS varied daily in response to the variation in air temperature; and the temperature on each day of the year was identical to the year prior. The temperatures below 15 m were essentially constant with time. Figure 11 shows the results of this simulation, displaying the temperature profile on the first of every other month. A second simulation was run to determine a steady temperature profile through the entire thickness of the MIS beneath the Pegasus Runway. The simulation started with the initial vertical profile temperature set at the annual average air temperature of -17.04°C . The surface temperature was fixed at the annual average temperature at McMurdo Station (-17.04°C), and the MIS bottom temperature was fixed

at a constant -1.7°C . The simulation was propagated through time until steady state was reached. Figure 11 also shows the results of this second simulation. The overall results indicate that at a 15 m depth, the temperature remains at a near constant temperature of -9.42°C and that the temperatures below this depth are steady and equal to the long-term steady temperature profile based on the annual average temperature at McMurdo Station and known bottom temperature.

Figure 11. Estimated temperature profile throughout the MIS beneath the Pegasus Runway.



3.4 Initial temperature profile

We used a novel approach to estimate the initial temperature profile through the Pegasus runway down to the 15 m depth. This approach is based on the analytic determination of the propagation of periodic oscillations of the surface temperature into the depth first given mathematical form by William Thomson (described in Carslaw and Jaeger [1980, 81]) combined with knowledge of the long-term steady temperature profile shown in Figure 11.

The approximate temperature at depth z on day j is then

$$T_j^z = \bar{T}^z + T_\delta + \sum_{n=1}^2 A_n e^{-\bar{k}z\sqrt{n}} \cos\left(\frac{n2\pi j}{365} - \varepsilon_n - \bar{k}z\sqrt{n}\right) \quad (29)$$

where \bar{T}^z is the steady state temperature at depth z (shown in Figure 11), T_δ is the mean temperature difference between McMurdo Station and Peg-asus Runway; and

$$\bar{k} = \frac{\sum_{i=1}^m \left(\frac{2\pi}{365} \frac{\rho_i C_p}{2k_i} \right)^{1/2} z_i}{z}$$

is a depth-averaged value of the thermal properties of the m layers from the surface to the depth z .

The results using this approach usually agreed to within 1°C–2°C of the long-term simulations described in the previous section.

4 Operational Field Data

Meteorological data collected at the Pegasus Runway was used as input to the Pegasus Runway vertical temperature model. The meteorological data included wind speed (m s^{-1}), air temperature ($^{\circ}\text{C}$), relative humidity (%), air pressure (mbar), downwelling solar radiation (W m^{-2}), and downwelling long-wave radiation (W m^{-2}). The U.S. Navy SPAWAR (Space and Naval Warfare Systems Command) Systems Center Atlantic, Polar Programs Integrated Process Team (<http://www.spawar.navy.mil/>), collected the data at 10-minute intervals. The data was transmitted to the Antarctic Meteorological Research Center at the University of Wisconsin (<http://amrc.ssec.wisc.edu/>) where it was then immediately available for our use. The measurement of the downwelling solar radiation was by an Eppley Precision Spectral Pyranometer (PSP) (The Eppley Laboratory, Inc., <http://www.eppleylab.com/>), which measures the sun and sky irradiance in the range of wavelengths from 0.285 to 2.8 μm . The measurement of the downwelling infrared radiation was by an Eppley Precision Infrared Radiometer (PIR), which measures wavelengths from 3.5 to 50 μm .

Using precision resistors, we measured the runway temperatures at 7 depths beneath the runway surface (4, 6, 8, 10, 12, 14, and 16 in.). The thermistors were placed at the centerline of the runway and 50 ft from the edge of the runway at 3000 and 7000 ft along the runway for a total of four measurement locations. The thermistors were installed by first cutting a small trench in the runway (Figure 12) that extended from the runway centerline to the runway edge. Vertical arrays of thermistors were placed in the trench at the runway centerline and 50 ft offset from the runway edge. The trenches were filled ice chips and snow, flooded with freshwater, and allowed to freeze. Finally, the snowcap was replaced on the surface of the ice. The thermistors were connected to a datalogger and the information transmitted by satellite phone at 1 hr intervals.

Figure 12. View of the trench used for installing temperature sensors in the runway.



5 Application

The Pegasus Runway vertical temperature model was used to simulate the vertical temperature profiles below the runway over three consecutive austral summers during periods when both meteorological data and runway temperature data were available. Table 3 lists the simulation start date and time and end date and time of each period. The model domain was established by dividing into layers the snow and ice composing the runway and the MIS beneath the runway down to a 15 m depth. In all simulations, the top 0.5 m was divided into layers of 0.01 m thickness, the next 0.5 m into layers of 0.05 m, and the remaining depth into layers of 0.10 m. The density, thermal conductivity, and bulk extinction coefficients were assigned to each layer based on the vertical distributions shown in Figures 7, 8, and 9. These values were kept constant during the simulations unless melting occurred. Then the density, thermal conductivity, and heat capacity were modified using equation (14).

Table 3. Simulation periods.

Start Date Time	End Date Time	Melt out
28 Dec 2011 2200	29 Jan 2012 1500	-
23 Dec 2012 0000	01 Jan 2013 0000	29 Dec 2012
29 Nov 2013 1250	05 Jan 2014 0320	31 Dec 2013

The first step of each simulation was to estimate the initial temperature at the upper and lower boundary of each layer of the solution grid at the start date and time by using the initial temperature procedure described above. The initial melt fraction was set to zero for each layer at the start of each simulation. The model was then propagated forward in time using 10-minute time steps. The observed air temperature, wind speed, relative humidity, barometric pressure, downwelling shortwave radiation, and downwelling long-wave radiation were used as inputs to the model. During periods of missing data, the values of these variables were held constant using the last available observation. The only exception was the downwelling shortwave radiation, which was modeled during periods of missing observations using

$$I_{s\downarrow} = c_1 S_0 \left(\frac{r_0}{r} \right)^2 \cos \theta_0 \quad (30)$$

where

- $I_{s\downarrow}$ = the estimated downwelling shortwave radiation;
- r = the daily distance between the earth and sun;
- r_0 = the mean distance between the earth and sun;
- S_0 = the solar constant at the mean Earth–Sun distance, $r_0 = 1369.3 \text{ W m}^{-2}$;
- θ_0 = the solar zenith angle;
- c_1 = an empirical constant to account for the impact of clouds ($c_1 = 0.75$).

The value of c_1 was estimated based on the observations of downwelling shortwave radiation made at the Pegasus Runway from 29 October 2010 until 5 February 2011. The solar zenith angle is a function of the runway location, the day of the year, and the time of day and was estimated using the procedure of Woolf (1968).

Table 4 lists the parameters used in the Pegasus Runway temperature model. Only the albedo reduction factor, α_{rf} , used to reduce the surface shortwave albedo during times of surface melt (equation [6]), and c_1 , the empirical constant used to account for the impact of clouds on the estimated downwelling solar radiation during periods of missing observations, equation (30), were determined empirically.

Table 4. Model Parameters.

Parameter	Value
Emittance of snow	0.97
Penetrating fraction of shortwave radiation	0.17
Bulk extinction coefficient blue ice	1.5 m^{-1}
Density of ice	916.8 kg m^{-3}
Density of water	1000 kg m^{-3}
Thermal conductivity of ice	$2.21 \text{ W (m }^{\circ}\text{C)}^{-1}$
Thermal conductivity of water	$0.58 \text{ W (m }^{\circ}\text{C)}^{-1}$
Heat capacity of ice	$2114 \text{ J (kg }^{\circ}\text{C)}^{-1}$
Heat capacity of water	$4181 \text{ J (kg }^{\circ}\text{C)}^{-1}$
Latent heat of fusion of water	330000 J kg^{-1}
Stefan-Boltzmann constant	$5.670 \times 10^{-8} \text{ W m}^{-2} \text{ K}^{-4}$

The observed runway temperatures were not used in estimating the initial vertical temperature profile at the start of each simulation period or at any

time during a simulation period. The observed runway temperatures were used only to determine the performance of the Pegasus Runway temperature model. The results of the simulations are described next.

5.1 2011–12 season

The Pegasus Runway temperature model was used to simulate the 2011–12 season from 28 December 2011 at 2200 hours (GMT) until 29 January 2012 at 1500 hours (GMT). Figure 13 shows the observed meteorological data used as input for the model. There were several periods of missing data. The only one of significant length was from 03 January 2012 at 1540 hours until 04 January 2012 at 2000 hours. During this period, we estimated input parameters as described in the introduction to this section. Figure 14 displays the observed runway temperatures, and Figure 15 shows the model results. In general, the simulation estimated the runway temperatures and their variations throughout the season quite well. Figure 16 displays the observed and simulated temperatures at the 4 in. depth, the depth closest to the runway surface; and Figure 17 provides the calculated temperature of the runway surface and the calculated liquid water fraction of the top surface layer and the layers immediately below the top surface. (The liquid water fraction scale is on the right axis of Figure 17. The liquid fraction result is for the surface and each layer immediately below the surface with a liquid water fraction greater than zero.) The temperature of the top surface reached 0°C on several occasions; but the length of time that the surface remained at 0°C was relatively short for each occasion, never lasting longer than a day. The simulation estimated that some liquid water formed at the surface and immediately below during each event as shown in Figure 17.

It is interesting to note that during this season, the model error goes through three phases with respect to time. These same phases can be seen at all depths, but our description concentrates on the 4 in. depth (Figure 16). During the first phase, lasting from about 28 December to 3 January, the model tended to be too cold compared to the observed. In the second phase, from about 3 January to 12 January, the model tended to be slightly warmer than the observations. In the third phase, the period after 12 January, the model is again slightly colder than the observations. The cause of these phases is not known. They probably result from changes in the runway conditions that impacted the heat budget of the runway. These changes could have resulted from variations in snow accumulation on the

runway through precipitation, snow drift, or sublimation; in the compaction, planning, or dragging operations performed; or in the surface albedo.

Figure 13. Meteorological conditions during the 2011–12 season.

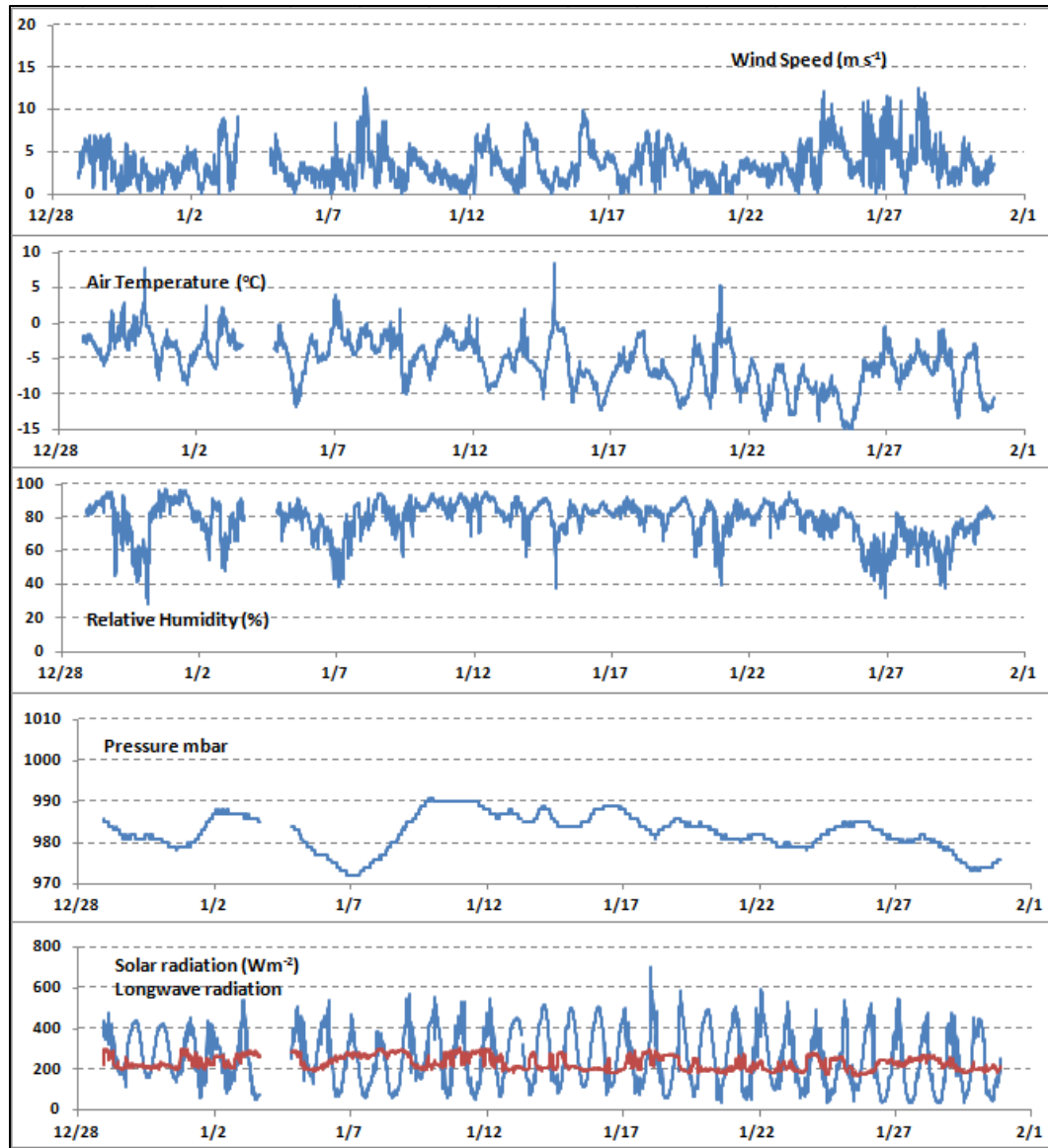


Figure 14. Observed runway temperatures during the 2011–12 season.

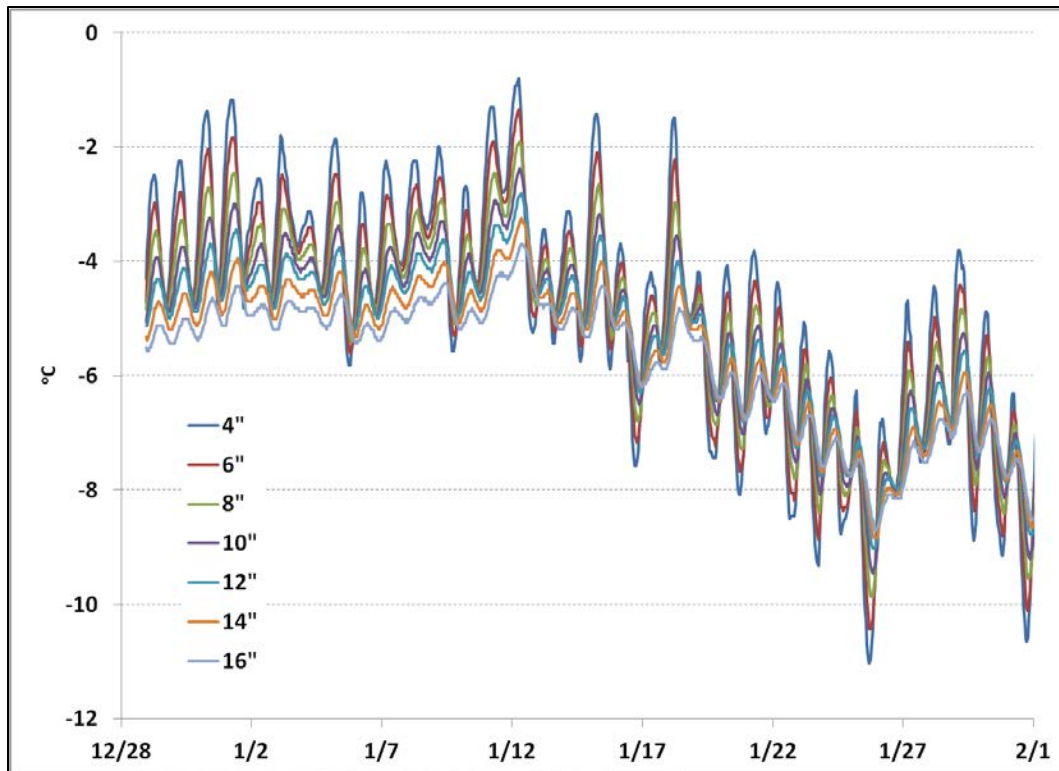


Figure 15. Modeled temperatures in the runway during the 2011–12 season.

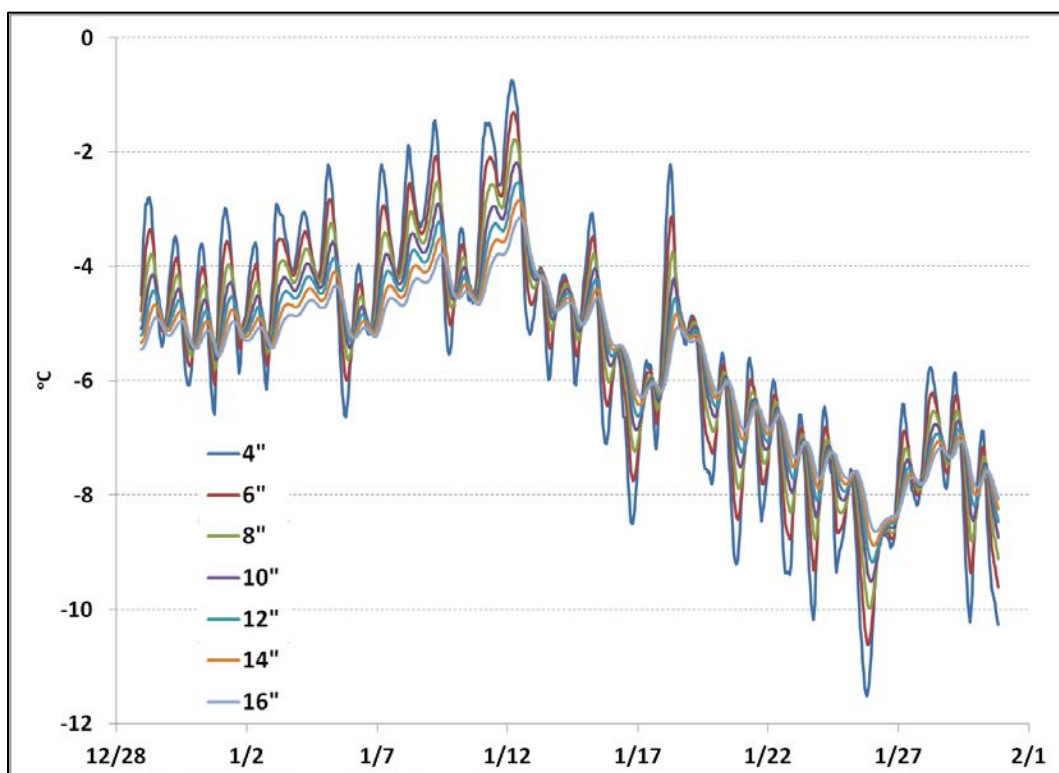


Figure 16. Observed and modeled temperature at a 4 in. depth.

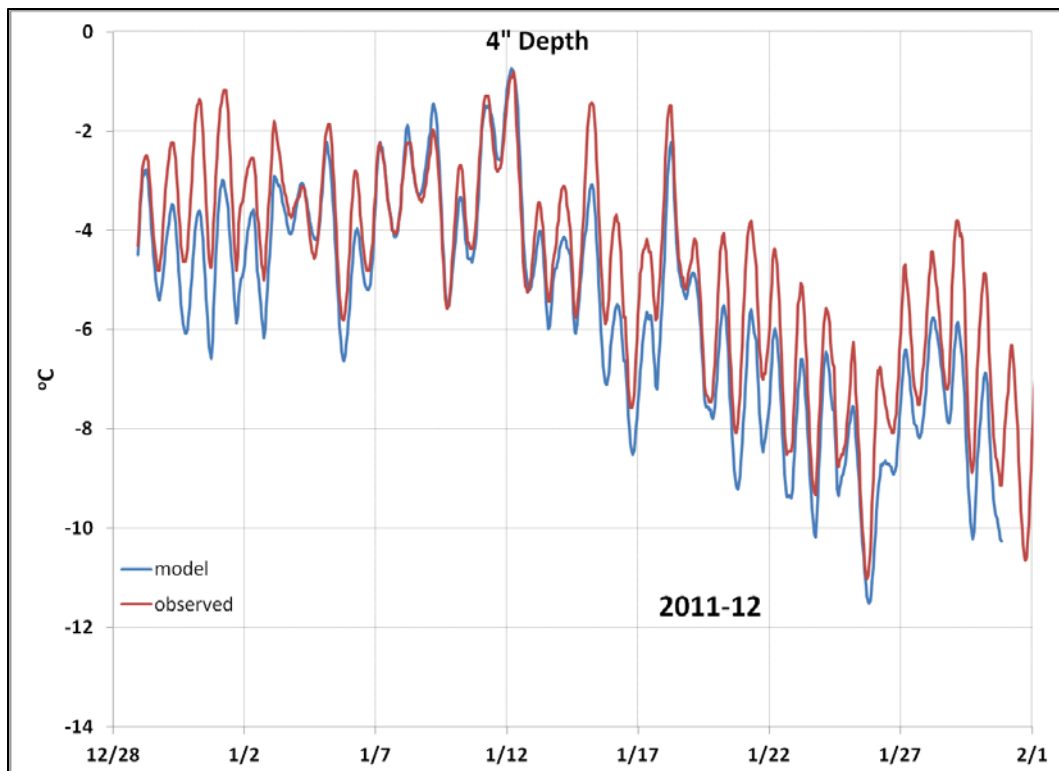


Figure 17. Modeled temperature and liquid water fraction at the surface.

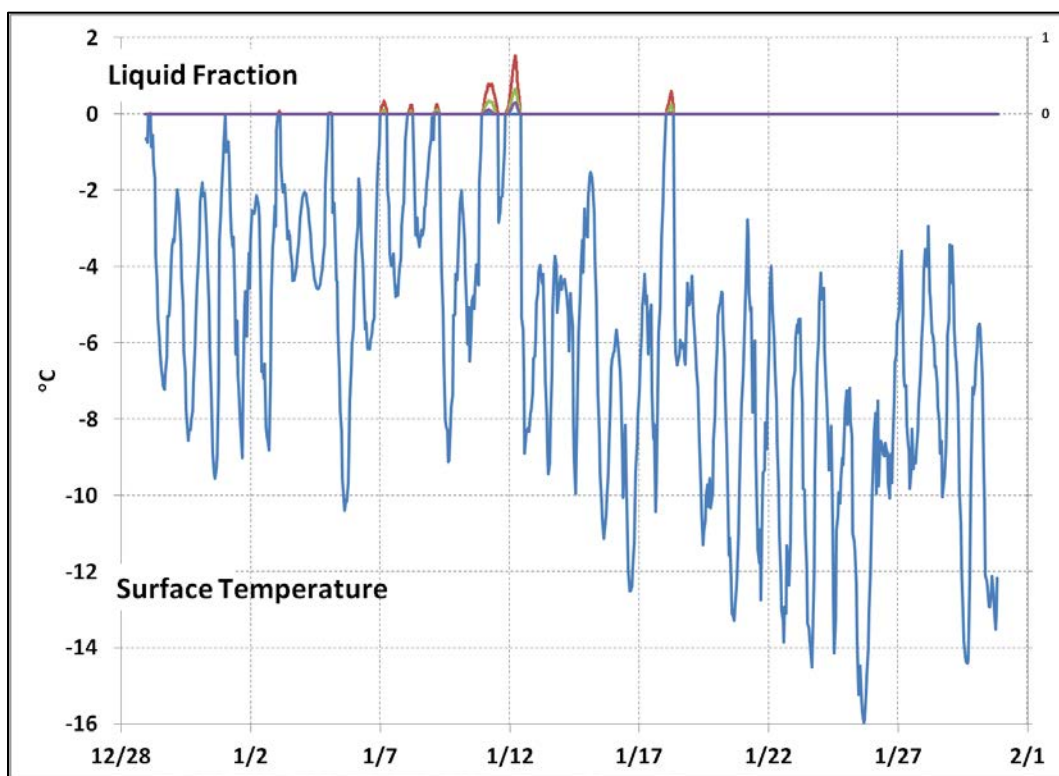


Table 5 lists the error statistics. The simulation model results were slightly negatively biased compared to the observed runway temperatures.

Table 5. Error statistics for the 2011–12 season.

	4 in. Depth	6 in. Depth	8 in. Depth	10 in. Depth	12 in. Depth	14 in. Depth	16 in. Depth
Bias	-0.85 °C	-0.67 °C	-0.54 °C	-0.43 °C	-0.35 °C	-0.17 °C	-0.02 °C
StDev	0.69 °C	0.61 °C	0.54 °C	0.48 °C	0.43 °C	0.39 °C	0.37 °C

5.2 2012–13 season

The Pegasus Runway temperature model was used to simulate the 2012–13 season from 23 December 2012 at 0000 hours (GMT) until 05 January 2014 at 0320 hours (GMT), when the runway melted to the point that the top-most runway temperature sensors were exposed to air and, therefore, the data was no longer valid. Figure 18 shows the observed meteorological data used as input for the model. There were no significant periods of missing data. Figure 19 displays the observed runway temperatures. Note that there is a general decline in the observed runway temperatures starting from their first reading until approximately 23 December. This two-day decline is thought to be an artifact resulting from the procedure used to install the temperature probes into the runway. It can also be seen that the observed runway temperatures increase more or less continuously until 01 January when the Pegasus Runway was closed to operations.

Figure 20 displays the model results. In general, the simulation estimates of the runway temperatures are reasonable. The model was able to reproduce quite well the temperature rise in the runway, and its timing, that led to the runway shutdown. Figure 21 displays the observed and simulated temperatures at the 4 in. depth, the depth closest to the runway surface. Figure 22 displays the calculated temperature of the runway surface and the calculated liquid water fraction of the top surface layer and the layers immediately below the top surface. (The liquid water fraction scale is on the right axis of Figure 22. The liquid water fraction result is for the surface and each layer immediately below the surface with a liquid water fraction greater than zero.) The temperature of the top surface reached 0°C on 27 December and consistently reached 0°C on each of the following days. Some liquid water was estimated to form at the surface and immediately below during each event as shown in Figure 22. Table 6 lists the error sta-

tistics. The simulation results were negatively biased compared to the observed runway temperatures.

Table 6. Error statistics for the 2012–13 season.

	4 in. Depth	6 in. Depth	8 in. Depth	10 in. Depth	12 in. Depth	14 in. Depth	16 in. Depth
Bias	-1.09 °C	-1.01 °C	-0.83 °C	-0.70 °C	-0.53 °C	-0.38 °C	-0.27 °C
StDev	1.29 °C	0.99 °C	0.76 °C	0.62 °C	0.58 °C	0.59 °C	0.63 °C

Figure 18. Meteorological conditions during the 2012–13 season.

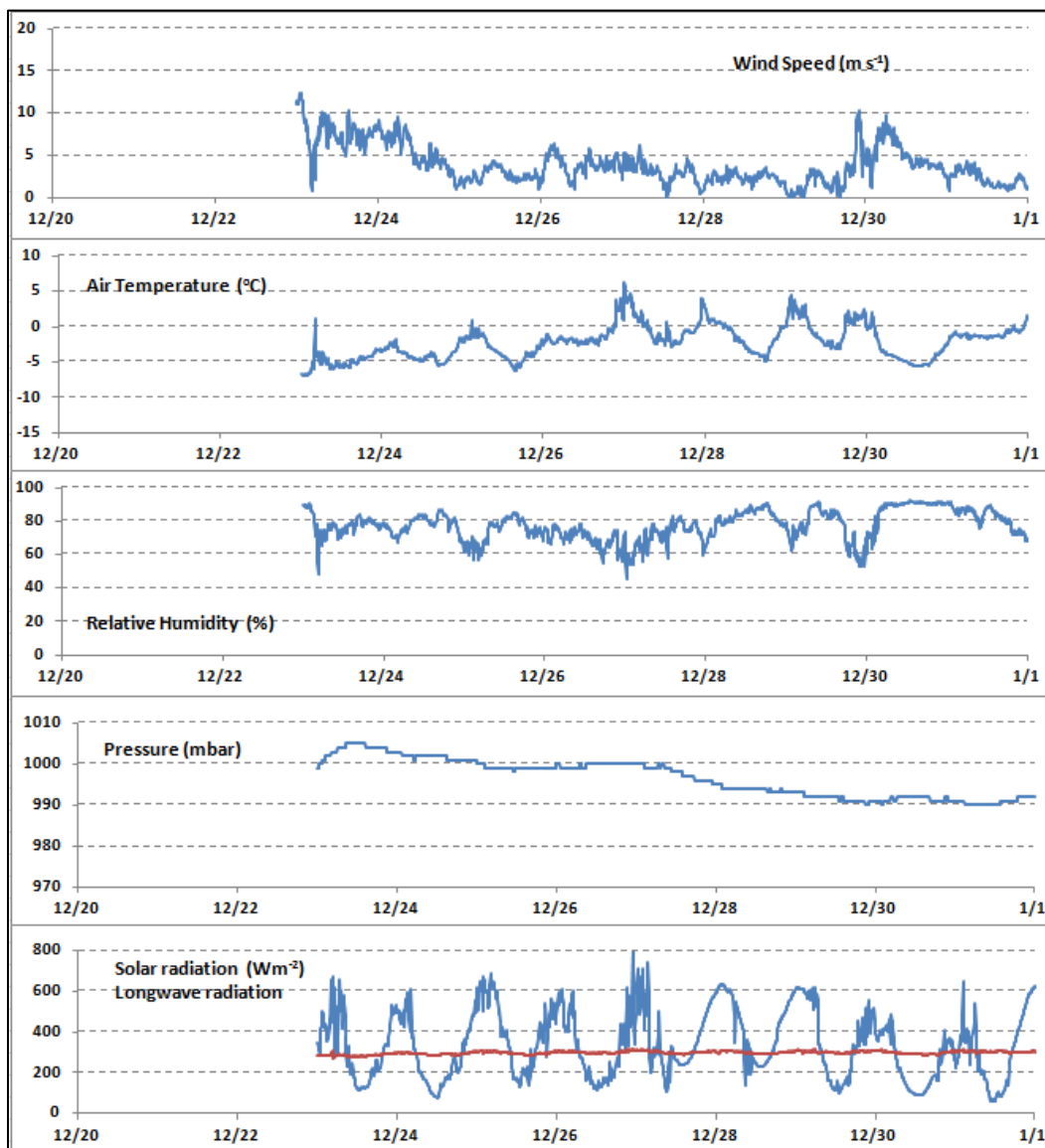


Figure 19. Observed temperatures in the runway during the 2012–13 season.

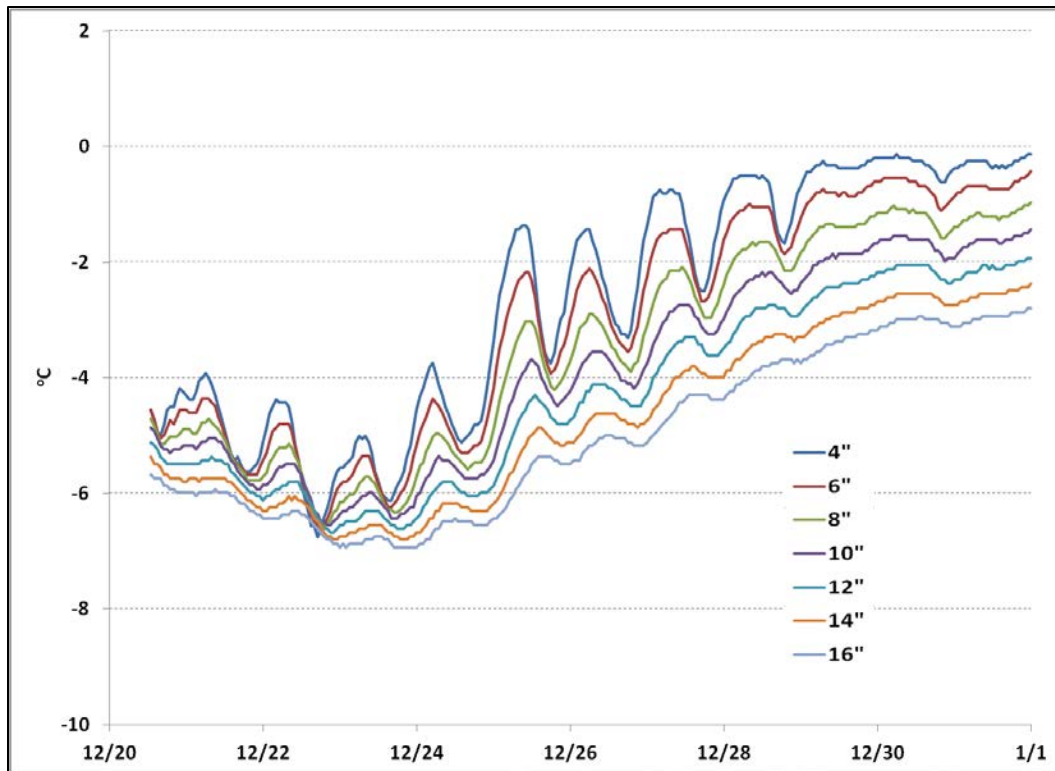


Figure 20. Modeled temperatures in the runway during the 2012–13 season.

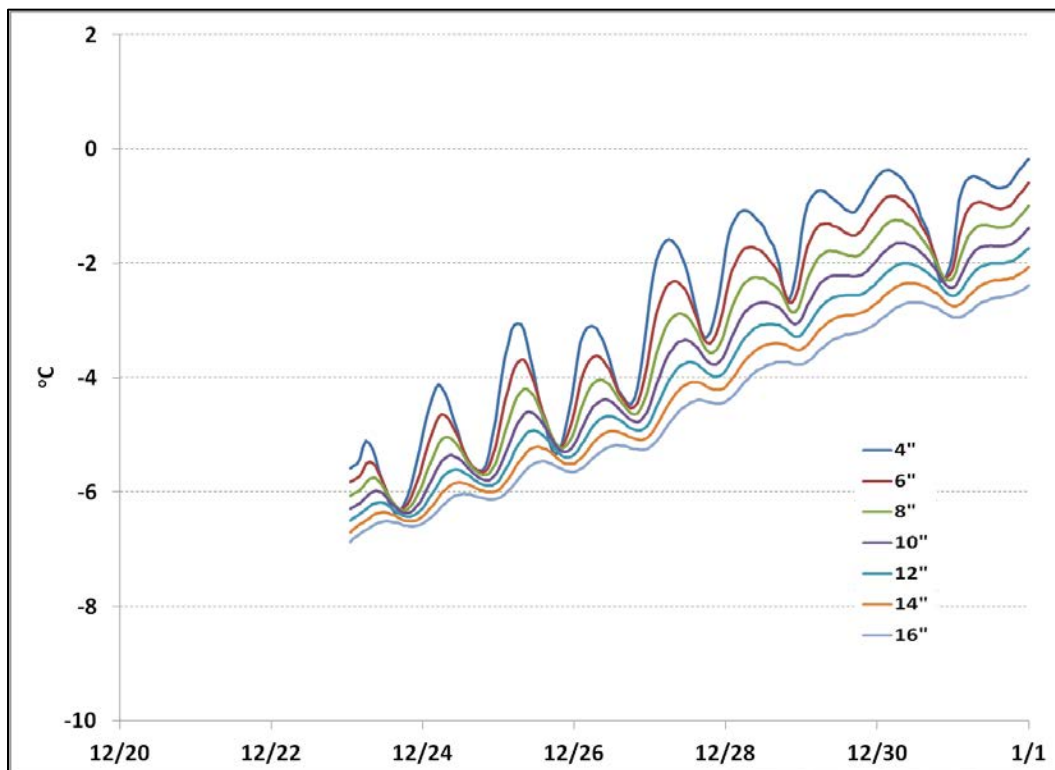


Figure 21. Observed and modeled temperature at a 4 in. depth.

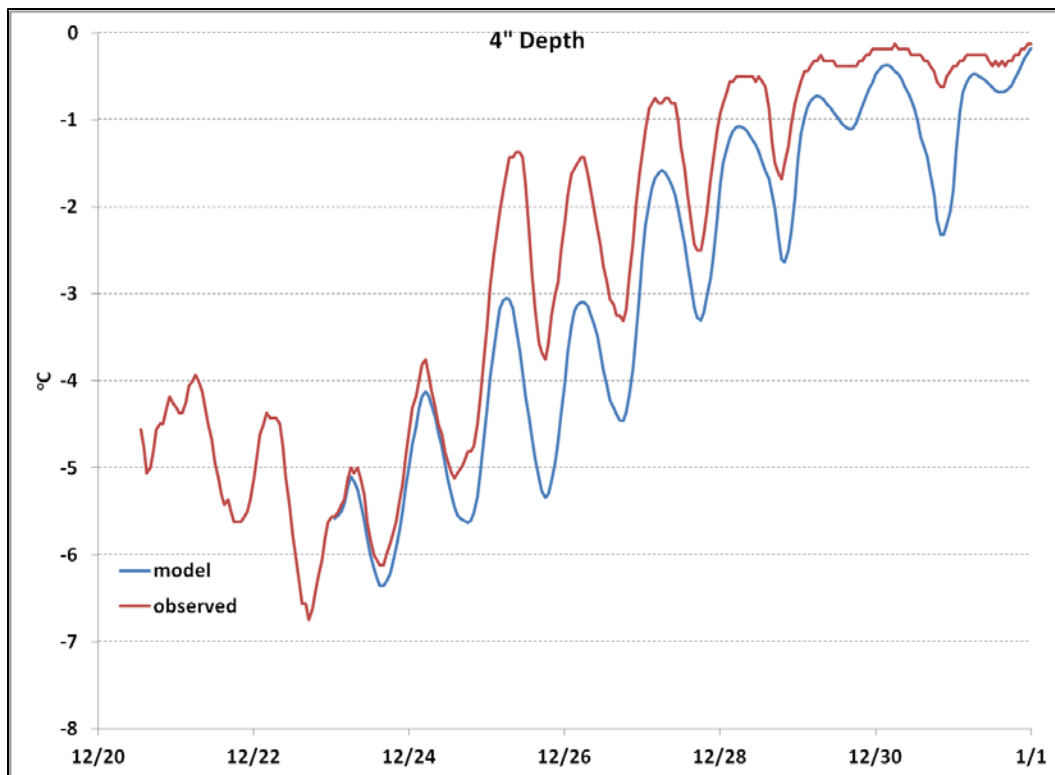
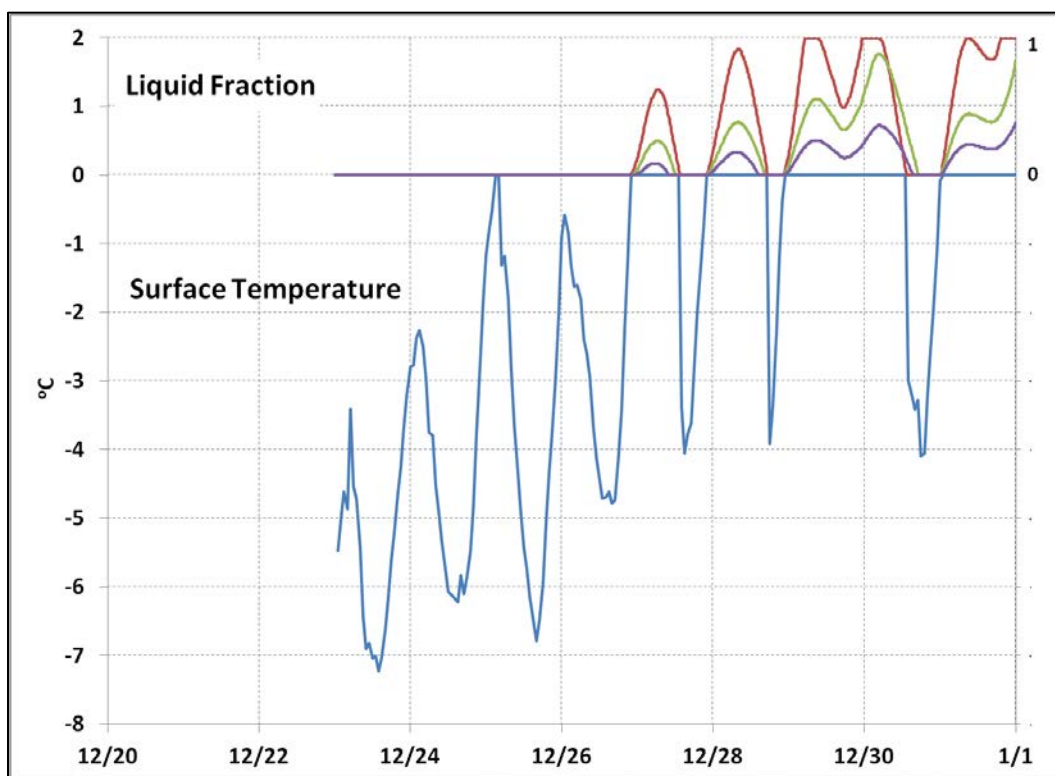


Figure 22. Modeled temperature and liquid water fraction at the surface.



5.3 2013–14 season

The Pegasus Runway temperature model simulated the 2013–14 season from 29 November 2013 at 1250 hours (GMT) until 1 January 2013 at 0000 hours (GMT), when the runway melted to the point that the topmost runway temperature sensors were exposed to air and, therefore, the data was no longer valid. Figure 23 shows the observed meteorological data used as input for the model. There were a number of periods of missing data, including one significant four-day period from 20 January until 23 January. In addition, we determined that the observations of the downwelling solar radiation were in error; therefore, we used estimated values for the entire simulation.

Figure 23. Meteorological conditions during the 2013–14 season.

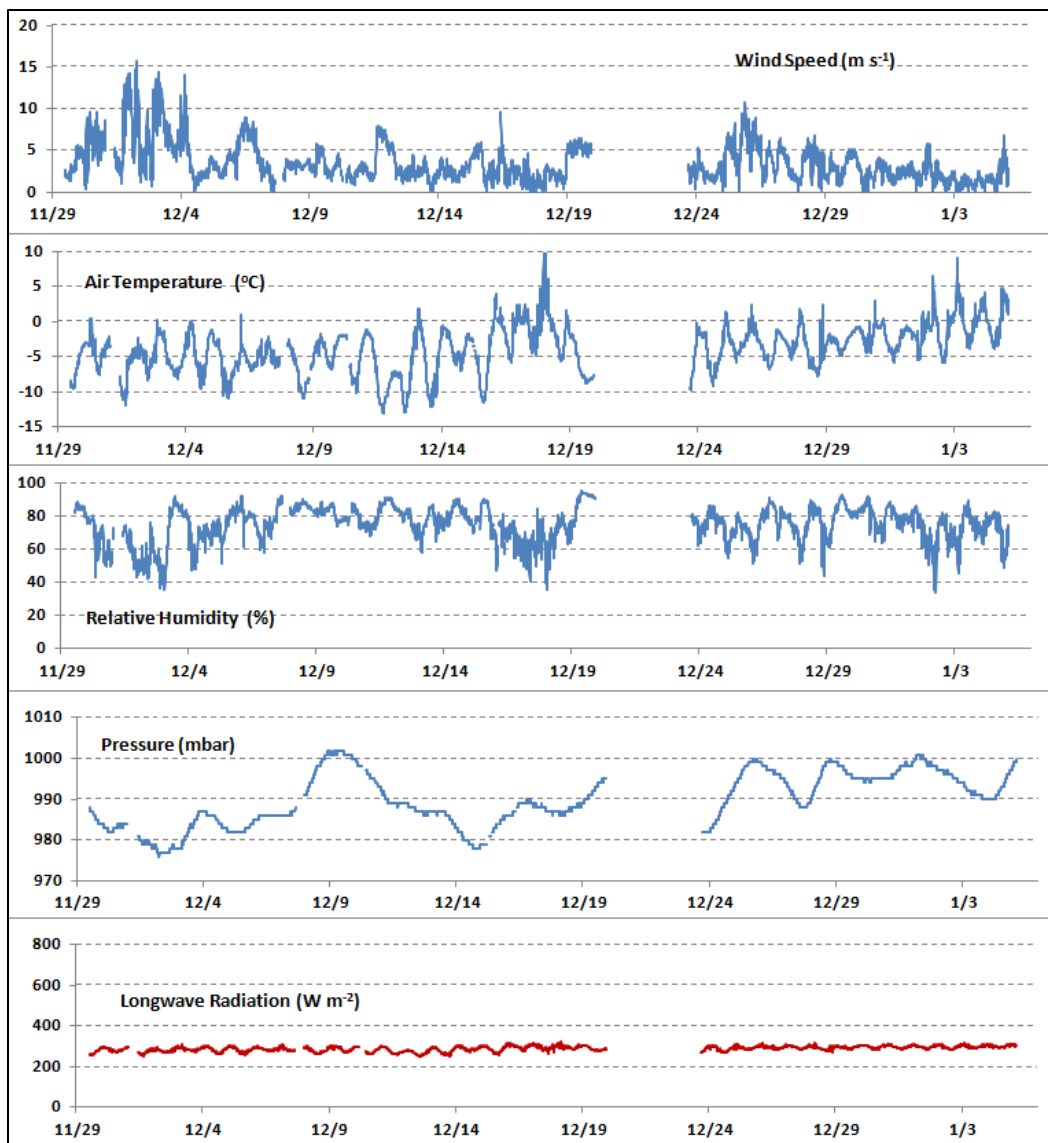


Figure 24 shows the observed runway temperatures, which begin on 6 December 2013. As in the previous season, there is a general decline in the observed runway temperatures, starting from their first reading and lasting approximately one day. As before, we assume this to be an artifact resulting from the procedure used to install the temperature probes into the runway. Additionally, the observed runway temperatures increase starting at the end of December and continuing until 04 January when the Pegasus Runway was closed to operations. Figure 25 displays the model results. The model simulation period started on 29 November, prior to the start of the observations. In general, the simulation's estimate of the runway temperatures is very good, especially considering the significant periods of missing meteorological data. The model was able to effectively reproduce the runway's temperature rise (and its timing) that lead to its shutdown. Figure 26 shows the observed and simulated temperatures at the 4 in. depth, the depth closest to the runway surface. Figure 26 provides the calculated temperature of the runway surface and the calculated liquid water fraction of the top surface layer and the layers immediately below the top surface. (The liquid water fraction scale is on the right axis of Figure 26. The liquid water fraction result is for the surface and each layer immediately below the surface with a liquid water fraction greater than zero.) The temperature of the top surface reached 0°C on several occasions and then was consistently at 0°C from 30 December onwards. Liquid water was estimated to form at the surface and immediately below during each occasion as shown in Figure 27. Table 7 lists the error statistics. The simulation results were slightly negatively biased above the 8 in. depth compared to the observed runway temperatures and slightly positively biased below that depth.

Table 7. Error statistics for the 2013–14 season.

	4 in. Depth	6 in. Depth	8 in. Depth	10 in. Depth	12 in. Depth	14 in. Depth	16 in. Depth
Bias	-0.53 °C	-0.19 °C	-0.08 °C	0.13 °C	0.32 °C	0.49 °C	0.72 °C
StDev	0.79 °C	0.71 °C	0.62 °C	0.55 °C	0.51 °C	0.47 °C	0.44 °C

Figure 24. Observed temperatures in runway during 2013–14 season.

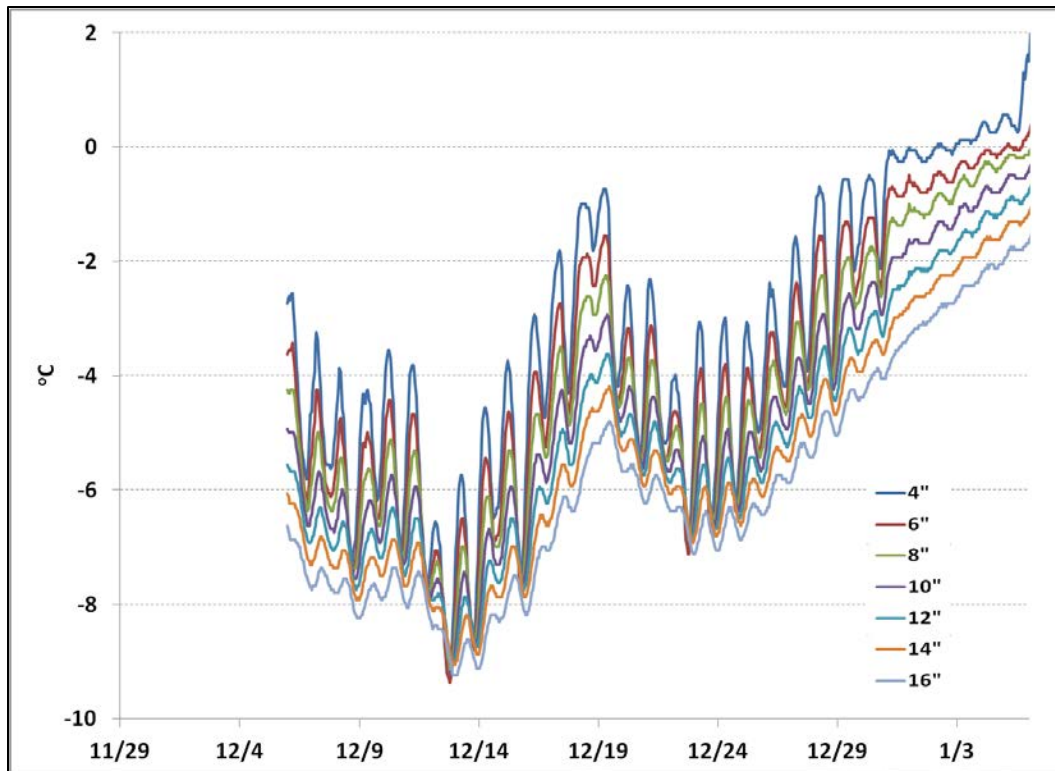


Figure 25. Modeled temperatures in runway during 2013–14 season.

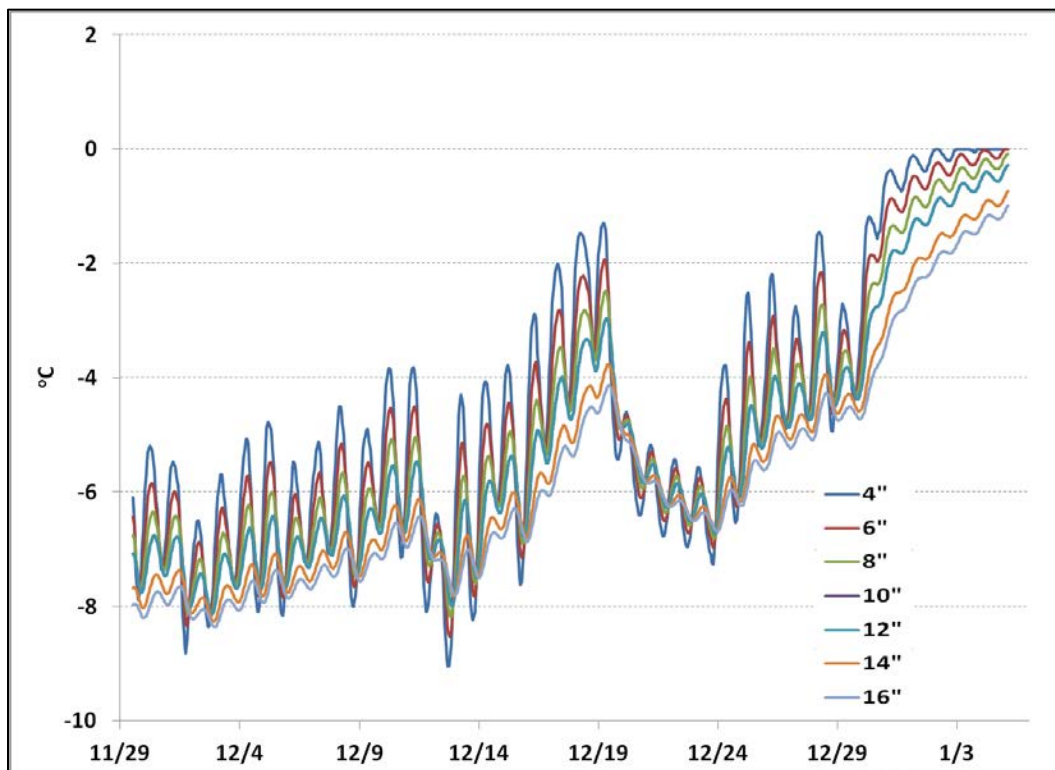


Figure 26. Observed and modeled temperature at a 4 in. depth.

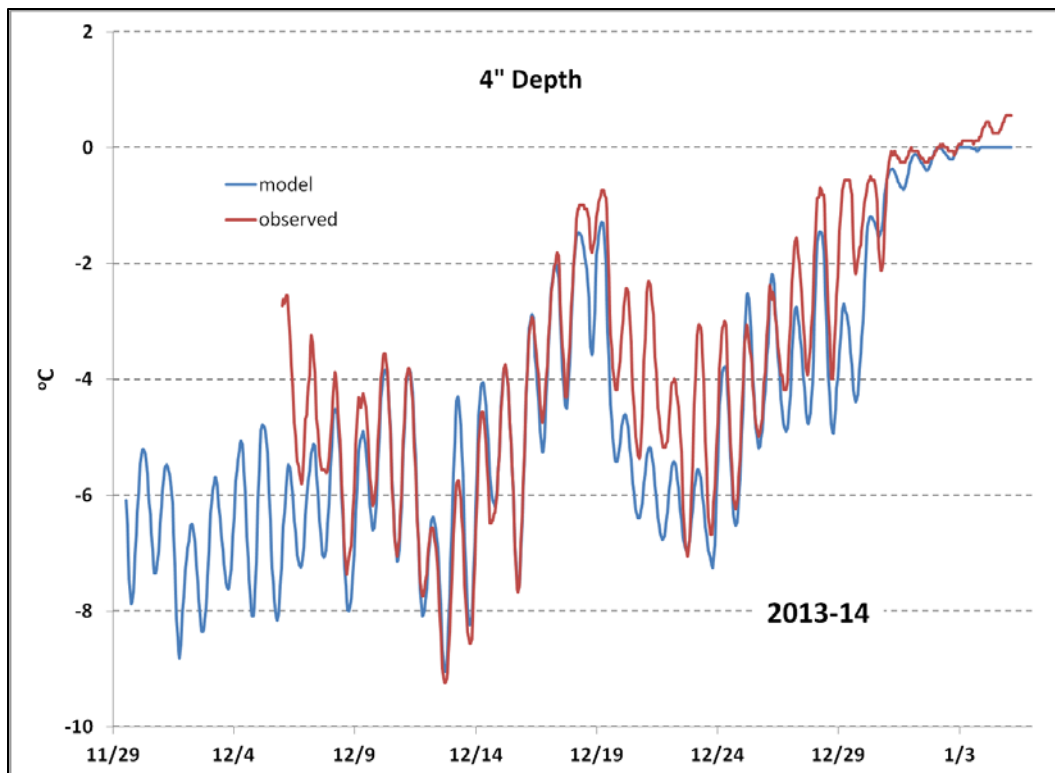
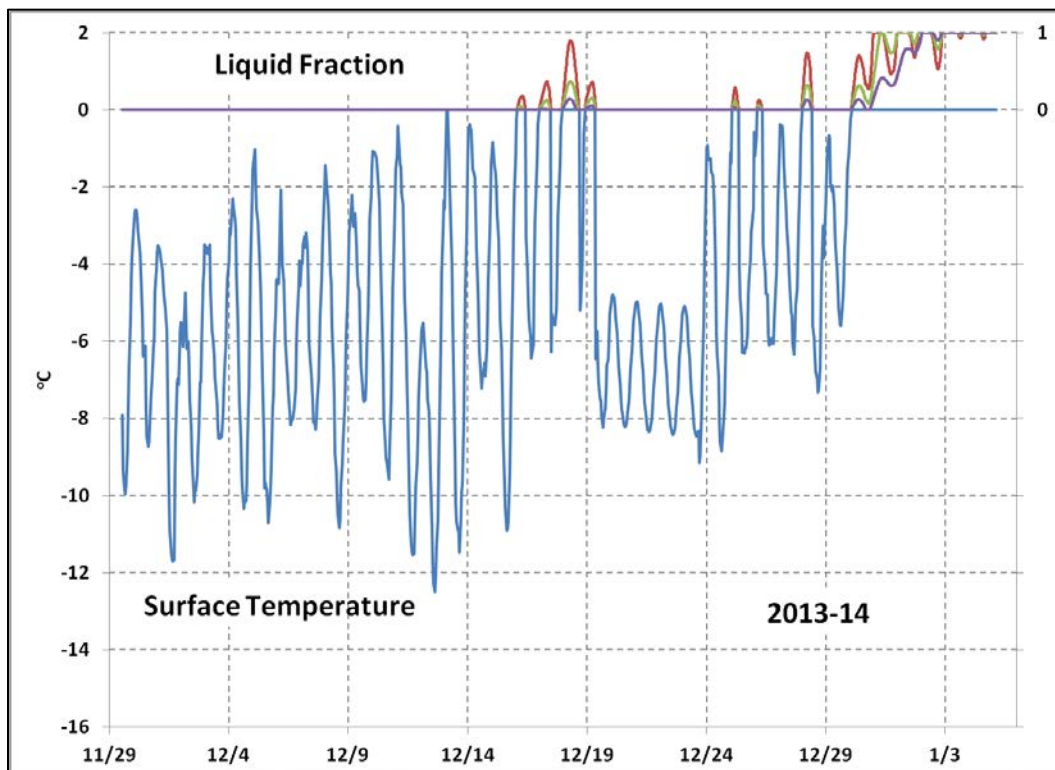


Figure 27. Modeled temperature and liquid water fraction at the surface.



6 Summary

The Pegasus Runway, located on the McMurdo Ice Shelf (MIS) 13 km south of McMurdo Station, is a unique runway composed of a compacted snowcap supported by a freshwater ice layer approximately 4.7 m thick. The runway is susceptible to weakening and reduction in the snowcap strength caused by warm weather and solar radiation. In the present work, we describe the development of a temperature model of the upper layers of the Pegasus Runway. This model is a major component of the system to forecast the occurrence of strength reduction in the airfield, which will be described in following reports.

To model the temperatures in the Pegasus runway, it is necessary to have a description of density, thermal conductivity, specific heat, and the broadband shortwave radiation extinction of the snow and ice that compose and underlay the runway. The surface albedo must be known, also. Measurements of these physical properties in the field are limited to density along with a few observations of broadband shortwave radiation extinction. The direct measurements of density made at the runway by us and others were confined to the top 5 m. Based on measurements made by others in the vicinity of the Pegasus Runway, we inferred the density deeper than 5 m. We then estimated the other physical properties based on the measured and estimated density and the layer type.

In all, there are four distinct layers of snow and ice at the runway between the surface and the bottom of the MIS: snowcap, superimposed ice, firn, and brine-saturated firn. Of the four distinct layers of snow and ice, the brine-saturated firn presented the greatest challenge with regard to heat transfer calculations. The presence of brine has a dramatic impact on the volumetric specific heat, especially at temperatures close to the ice/sea water equilibrium temperature and high salinities. In practice, the specific heat of brine-saturated firn could be estimated if the brine fraction and brine salinity were known. These properties are not known beneath the Pegasus Runway. If we assumed that the brine-saturated firn was formed when the original dry firn (with an estimated density determined either by depth or overburden pressure) was flooded with seawater (with known salinity), we could estimate the properties of the brine-saturated firn. Unfortunately, measurements of the properties of the brine-saturated firn in

the vicinity of Pegasus Runway do not present a consistent picture of the original brine salinity. We approximate the thermal properties of the brine-saturated firn based on the properties of ice with bubbles as described by equation (8). This approximation is justified given the relative depth of the brine-saturated firn. Below 15 m to the base of the MIS, the temperature does not change with time; and the specific heat does not appear in the thermal calculations. Between 15 m and the top of the brine-saturated firn at 9 m, the ice is cold; and the brine has less impact on the thermal properties. Overall we assumed that the saturated brine layer has the thermal conductivity of ice with a density of 880 kg m^{-3} and a resultant thermal conductivity of $2.13 \text{ W (m }^{\circ}\text{C})^{-1}$.

The estimated thermal properties of the four distinct layers of snow and ice at the runway allowed the model to accurately simulate the observed runway temperatures, showing that the assumptions made for the properties of the brine-saturated firn were appropriate. Our technique for estimating the initial temperature profile at startup worked well by using empirical modifications to the classic mathematical description of propagation of periodic oscillations of surface temperature. The broadband shortwave albedo of the runway was developed based on field measurements made during the winter of 2010–11 of the downwelling and upwelling shortwave radiation. We found that the parameterization proposed by Dickinson et al. (1986) described the albedo well as a function of the solar angle. We reduced the surface albedo at a time-constant rate when the liquid water fraction of the surface layer was greater than zero. This allowed accurate simulation of the meltout of the runway in the 2012–13 and 2013–14 seasons.

The model of the temperature within the Pegasus Runway compares very well to the temperatures measured in the field. In almost all cases, the average error at each depth is less than 1.0°C . In general, the average error (bias) becomes less negative with depth. Of the three simulated seasons, the 2011–12 season provides the longest period of time for comparison. It is interesting to note that during this season, the model error goes through three phases with respect to time. These same phases can be seen at all depths. During the first phase, lasting from about 28 December to 3 January, the model tended to be too cold compared to the observed. In the second phase, from about 3 January to 12 January, the model tended to be slightly warmer than the observations. In the third phase, the period after 12 January, the model was again slightly colder than the observations. We

do not know the cause of these phases, but they probably result from changes in the runway conditions that impact the heat budget of the runway but that are not adequately captured in the model. These changes could have resulted from changes in snow accumulation on the runway through precipitation, snow drift, or sublimation; changes in the compaction, planning, or dragging operations performed; or changes in the surface albedo.

References

Andreas, E. L. 1987. A theory for the scalar roughness and the scalar transfer coefficients over snow and sea ice. *Boundary-Layer Meteorology* 38:159–184.

Andreas, E. L. 1996. *The Atmospheric Boundary Layer over Polar Marine Surfaces*. Monograph 96-2. Hanover, NH: U.S. Army Cold Regions Research and Engineering Laboratory.

Andreas, E. L. 1998. The atmospheric boundary layer over polar marine surfaces. In *Physics of Ice-Covered Seas*, Vol. 2, ed. M. Leppäranta, 715–773. Helsinki, Finland: Helsinki University Press.

Andreas, E. L. 2002. Parameterizing Scalar Transfer over Snow and Ice: A Review. *Journal of Hydrometeorology* 3:417–432.

Andreas, E. L. 2005. *Handbook of Physical Constants and Functions for Use in Atmospheric Boundary Layer Studies*. ERDC/CRREL M-05-1. Hanover, NH: U.S. Army Engineer Research and Development Center.

Andreas, E. L., and K. J. Claffey. 1995. Air-ice drag coefficients in the western Weddell Sea: 1. Values deduced from profile measurements. *Journal of Geophysical Research* 100 (C3): 4821–4831.

Arcone, S. A., A. J. Delaney, and W. Tobiasson. 1994. *Subsurface Radar Investigations at the Pegasus Glacial-Ice Runway and Williams Field, McMurdo Station, Antarctica*. CRREL Report 94-12. Hanover, NH: U.S. Army Cold Regions Research and Engineering Laboratory.

Ashton, G. D. 1986. *River and Lake Ice Engineering*. Littleton, CO: Water Resources Publications.

Bintanja, R., and M. R. van den Broeke. 1995. The Surface Energy Balance of Antarctic Snow and Blue Ice. *Journal of Applied Meteorology* 34:902–926.

Blaisdell, G. L., and R. M. Lang. 1995. Pegasus: a glacial-ice runway for wheeled flight operations at McMurdo Station. *Antarctic journal of the United States* 30 (1–4): 7–10. <http://www.nsf.gov/pubs/1996/nsf96120/nsf96120.pdf>.

Blaisdell, G. L., V. Klokov, and D. Diemand. 1992. Development of a wheeled runway for McMurdo on the Ross Ice Shelf. In *Standing Committee on Antarctic Logistics and Operations (SCALOP) Report of Meeting Bariloche, Argentina, 8-12 June*.

Blaisdell, G. L., R. M. Lang, G. Crist, K. Kurtti, R. J. Harbin, and D. Flora. 1998. *Construction, maintenance, and operation of a glacial runway, McMurdo Station, Antarctica*. Monograph 98-01. Hanover, NH: U.S. Army Cold Regions Research and Engineering Laboratory. <http://acwc.sdp.sirsi.net/client/search/asset/1001388>.

Brandt, R. E., and S. G. Warren. 1993. Solar-heating rates and temperature profiles in Antarctic snow and ice. *Journal of Glaciology* 39 (131): 99–110.

Carslaw, H. S., and J. C. Jaeger. 1980. *Conduction of Heat in Solids*. Oxford, UK: Oxford University Press.

Cox, G. F. N., and W.F. Weeks. 1983. Equations for determining the gas and brine volumes in sea ice samples. *Journal of Glaciology* 29 (102): 306–16.

Cragin, J. H., A. J. Gow, and A. Kovacs. 1983. *Chemical fractionation of brine in the McMurdo Ice Shelf, Antarctica*. CRREL Report 83-6. Hanover, NH: U.S. Army Cold Regions Research and Engineering Laboratory.

Deardorff, J. W. 1970. Convective velocity and temperature scales for the unstable planetary boundary layer and for Rayleigh convection. *Journal of the Atmospheric Sciences* 27:1211–1213.

Dickinson, R. E., A. Henderson-Sellers, P. J. Kennedy, and M. F. Wilson. 1986. *Biosphere-Atmosphere Transfer Scheme (BATS) for the NCAR Community Climate Model*. NCAR Technical Note 275. Boulder, CO: National Center for Atmospheric Research.

Douville, H., J.-F. Royer, J.-F. Mahfouf. 1995. A new snow parameterization for the Météo-France climate model. Part I: validation in stand-alone experiments. *Climate Dynamics* 12:21–35.

Dunbar, G. B., N. A. N. Bertler, and R. M. McKay. 2009. Sediment flux through the McMurdo Ice Shelf in Windless Bight, Antarctic. *Global and Planetary Change* 69 (3): 87–93.

Fairall, C. W., E. F. Bradley, D. P. Rogers, J. B. Edson, and G. S. Young. 1996. Bulk parameterization of air-sea fluxes for Tropical Ocean-Global Atmosphere Coupled-Ocean Atmosphere Response Experiment. *Journal of Geophysical Research* 101:3747–3764.

Flato, G., and R. D. Brown. 1996. Variability and climate sensitivity of landfast Arctic sea ice. *Journal of Geophysical Research* 101 (C10): 25,767–25,777.

Gardner, A. S., and M. J. Sharp. 2010. A review of snow and ice albedo and the development of a new physically based broadband albedo parameterization. *Journal of Geophysical Research* 115:F01009.

Grenfell, T. C., and G. A. Maykut. 1977. The optical properties of ice and snow in the arctic basin. *Glaciology* 18:445–463.

Haehnel, R. B., K. Bjella, M. A. Knuth, and L. Barna. 2013. *McMurdo Consolidated Airfields Study: Phase I, Basis of Design*. ERDC/CRREL TR-13-5. Hanover, NH: U.S. Army Engineer Research and Development Center.

Heine, A. J. 1968. Brine in the McMurdo ice shelf, Antarctica. *New Zealand Journal of Geology and Geophysics* 11 (4): 829–839.

Henneman, H. E., and H. G. Stefan. 1999. Albedo models for snow and ice on a freshwater lake. *Cold Regions Science and Technology* 29 (1): 31–48.

Holtslag, A. A. M., and H. A. R. De Bruin. 1988. Applied modeling of the nighttime surface energy balance over land. *Journal of Applied Meteorology* 27: 689–704.

Jordan, R. E., E. L Andreas, and A. P. Makshtas. 1999. Heat budget of snow-covered sea ice at North Pole 4. *Journal of Geophysical Research* 104:7785–7806.

Jordan, R. E., E. L Andreas, and A. P. Makshtas. 2001. Modeling the surface energy budget and the temperature structure of snow and brine-snow at Ice Station Weddell. In *Preprints, Sixth Conference on Polar Meteorology and Oceanography, San Diego, CA*, 129–132. Boston, MA: American Meteorological Society.

Klokov, V., and D. Diemand. 1995. Glaciology of the McMurdo Ice Shelf in the area of air operations. In *Contributions to Antarctic research IV*, ed. D. H. Elliot and G. L. Blaisdell. Washington, DC: American Geophysical Union.

Kovacs, A., and A. J. Gow. 1975. Brine infiltration in the McMurdo Ice Shelf, McMurdo Sound, Antarctica. *Journal of Geophysical Research* 80:1957–1961.

Kovacs, A., A. J. Gow, J. H. Cragin, and R. M. Morey. 1982. *The brine zone in the McMurdo Ice Shelf, Antarctica*. CRREL Report 82-39. Hanover, NH: U.S. Army Cold Regions Research and Engineering Laboratory.

Liston, G. E., O. Bruland, H. Elvehøy, and K. Sand. 1999. Below-surface ice melt on the coastal Antarctic ice sheet. *Journal of Glaciology* 45 (150): 273–285.

Liu, W. T., K. B. Katsaros, and J. A. Businger. 1979. Bulk parameterization of air-sea exchanges of heat and water vapor including the molecular constraints at the interface. *Journal of the Atmospheric Sciences* 36:1722–1735.

Maykut, G. A. 1982. Large-Scale heat exchange and Ice Production in the Central Arctic. *Journal of Geophysical Research* 87 (C10): 7971–7984.

McCrae, I. R. 1984. *A summary of glaciological measurements made between 1960 and 1984 on the McMurdo Ice Shelf, Antarctica*. School of Engineering Report 360. Auckland, New Zealand: University of Auckland, Department of Theoretical and Applied Mechanics.

Mellor, M. 1988. *Hard surface runways in Antarctica*. Special Report 88-13. Hanover, NH: U.S. Army Cold Regions Research and Engineering Laboratory.

Mellor, M., and C. Swithinbank. 1989. Airfields on Antarctic glacier ice. CRREL Report 89-21. Hanover, NH: U.S. Army Cold Regions Research and Engineering Laboratory.

Ono, N. 1967. Specific Heat and Heat of Fusion of Sea Ice. In *Physics of Snow and Ice: proceedings* 1 (1): 599–610. <http://hdl.handle.net/2115/20328>.

Paige, R. A. 1968. Sub-surface melt pools in the McMurdo ice Shelf, Antarctica. *Journal of Glaciology* 7 (51): 511–516.

Paterson, W. S. B. 1994. *The Physics of Glaciers*. 3rd ed. Tarrytown, NY: Pergamon/Elsevier Science Inc.

Paulson, C. A. 1970. The mathematical representation of wind speed and temperature profiles in the unstable atmospheric surface layer. *Journal of Applied Meteorology* 9:857–861.

Rack, W., C. Haas, and P. J. Langhorne. 2013. Airborne thickness and freeboard measurements over the McMurdo Ice Shelf, Antarctica, and implications for ice density. *Journal of Geophysical Research: Oceans* 118 (11): 5899–5907.

Risk, G. F., and M. P. Hochstein. 1967. Subsurface measurements on the McMurdo Ice Shelf, Antarctica. *New Zealand Journal of Geology and Geophysics* 10 (2): 484–497.

Schlatter, T. W. 1972. The local surface energy balance and subsurface temperature regime in Antarctica. *Journal of Applied Meteorology* 11 (7): 1048–1062.

Schwerdtfeger, P. 1963. The thermal properties of sea ice. *Journal of Glaciology* 4 (36): 789–807.

Stern, A. A., M. S. Dinniman, V. Zagorodnov, S. W. Tyler, and D. M. Holland. 2013. Intrusion of warm surface water beneath the McMurdo Ice Shelf, Antarctica. *Journal of Geophysical Research: Oceans* 118 (12): 7036–7048.

Stuart, A. W., and C. Bull. 1963. Glaciological observations on the Ross ice Shelf near Scott Base, Antarctica. *Journal of Glaciology* 4:399–413.

Sturm, M., J. Holmgren, M. Konig, K. Morris. 1997. The thermal conductivity of seasonal snow. *Journal of Glaciology* 43 (143): 26–41.

Swithinbank, C. 1970. Ice movement in the McMurdo Sound area of Antarctica. In *International Symposium on Antarctic Glaciological Exploration (ISAGE), Hanover, NH, 3–7 September 1968*, 86:472–487. International Association of Scientific Hydrology.

Woolf, H. M. 1968. *On the computation of solar elevation angles and the determination of sunrise and sunset times*. NASA TM X-1646. Washington, DC: National Aeronautics and Space Administration.

Yen, Y.-C., K. C. Cheng, and S. Fukusako. 1992. A Review of Intrinsic Thermophysical Properties of Snow, Ice, Sea Ice, and Frost. *The Northern Engineer* 23 (4) and 24 (1).

REPORT DOCUMENTATION PAGE

Form Approved
OMB No. 0704-0188

Public reporting burden for this collection of information is estimated to average 1 hour per response, including the time for reviewing instructions, searching existing data sources, gathering and maintaining the data needed, and completing and reviewing this collection of information. Send comments regarding this burden estimate or any other aspect of this collection of information, including suggestions for reducing this burden to Department of Defense, Washington Headquarters Services, Directorate for Information Operations and Reports (0704-0188), 1215 Jefferson Davis Highway, Suite 1204, Arlington, VA 22202-4302. Respondents should be aware that notwithstanding any other provision of law, no person shall be subject to any penalty for failing to comply with a collection of information if it does not display a currently valid OMB control number. **PLEASE DO NOT RETURN YOUR FORM TO THE ABOVE ADDRESS.**

1. REPORT DATE (DD-MM-YYYY) January 2015			2. REPORT TYPE Technical Report/Final		3. DATES COVERED (From - To)	
4. TITLE AND SUBTITLE Vertical Temperature Simulation of Pegasus Runway, McMurdo Station, Antarctica					5a. CONTRACT NUMBER	
					5b. GRANT NUMBER	
					5c. PROGRAM ELEMENT NUMBER	
6. AUTHOR(S) Steven F. Daly, Robert Haehnel, and Christopher Hiemstra					5d. PROJECT NUMBER	
					5e. TASK NUMBER EP-ANT-14-51	
					5f. WORK UNIT NUMBER	
7. PERFORMING ORGANIZATION NAME(S) AND ADDRESS(ES) Cold Regions Research and Engineering Laboratory (CRREL) U.S. Army Engineer Research and Development Center (ERDC) 72 Lyme Road Hanover, NH 03755-1290					8. PERFORMING ORGANIZATION REPORT NUMBER ERDC/CRREL TR-15-2	
9. SPONSORING / MONITORING AGENCY NAME(S) AND ADDRESS(ES) National Science Foundation, Division of Polar Programs Antarctic Infrastructure and Logistics Arlington, VA 22230					10. SPONSOR/MONITOR'S ACRONYM(S) NSF	
					11. SPONSOR/MONITOR'S REPORT NUMBER(S)	
12. DISTRIBUTION / AVAILABILITY STATEMENT Approved for public release; distribution is unlimited.						
13. SUPPLEMENTARY NOTES Engineering for Polar Operations, Logistics, and Research (EPOLAR)						
14. ABSTRACT Pegasus Runway, located 13 km south of McMurdo Station, Antarctica, on the McMurdo Ice Shelf (MIS), is constructed out of snow and ice. It is susceptible to weakening and damage caused by melting and to reduction in the strength caused by warm weather and sunlight. This report describes the development of the Pegasus Runway temperature model. It begins by quantitatively describing the physical properties of the Pegasus Runway snow and ice and the physical properties of the MIS directly beneath the runway. The temperature model is based on a one-dimensional heat conduction model that includes the penetration and absorption of solar radiation beneath the surface. The report describes the methods for estimating the sensible heat, latent heat, shortwave radiation, and long-wave radiation surface heat fluxes that drive the model and presents estimates of the constant-temperature lower-boundary condition for the model. A novel approach for estimating the initial vertical temperature profile is used. We simulate the Pegasus Runway temperatures for three austral summer seasons (2011–12, 2012–13, and 2013–14). The model simulation shows good results when compared to in situ observations of the runway temperatures.						
15. SUBJECT TERMS Albedo Antarctica		EPOLAR Ice properties McMurdo ice sheet		NSF Runway Temperature modeling		
16. SECURITY CLASSIFICATION OF: a. REPORT Unclassified			17. LIMITATION OF ABSTRACT SAR	18. NUMBER OF PAGES 67	19a. NAME OF RESPONSIBLE PERSON	
b. ABSTRACT Unclassified					19b. TELEPHONE NUMBER (include area code)	
Standard Form 298 (Rev. 8-98) Prescribed by ANSI Std. Z39-18						